Progress in Surface Science 85 (2010) 1–27

Contents lists available at ScienceDirect

Progress in Surface Science

journal homepage: www.elsevier.com/locate/progsurf

Review

Creation, electronic properties, disorder, and melting of two-dimensional surface-state-mediated adatom superlattices

Markus Ternes [a,b,*], Marina Pivetta [a], François Patthey [a], Wolf-Dieter Schneider [a]

[a] *Ecole Polytechnique Fédérale de Lausanne (EPFL), Institut de Physique de la Matiére Condensée, CH-1015 Lausanne, Switzerland*
[b] *Max-Planck Institute for Solid State Research, Heisenbergstr. 1, D-70569 Stuttgart, Germany*

ARTICLE INFO

Commissioning Editor P.M. Echenique

Keywords:
Two-dimensional superlattice
Adatom interaction
Surface-state-mediated interactions
Two-dimensional melting
Scanning tunneling microscopy
Scanning tunneling spectroscopy

ABSTRACT

Surface-state-mediated interactions influence the spatial distribution of adatoms at surfaces. These indirect interactions are the driving force for the creation of superlattices of individual adsorbed atoms when the adatom concentration, the sample temperature, and the adatom diffusion barrier are in a subtle balance, as it has been first reported for Ce adatoms on Ag(1 1 1). The conditions for the formation of such superlattices are discussed. Specifically, the adatom concentration is shown to modify considerably the electronic structure of the Ag(1 1 1) surface. With increasing temperature the superlattice undergoes a direct transition from a two-dimensional solid to a two-dimensional liquid. Such superlattices, consisting of magnetic adatoms, may be interesting as model systems for the study of direct and indirect magnetic interactions in two dimensions.

Contents

---

[*] Corresponding author. Address: Max-Planck Institute for Solid State Research, Heisenbergstr. 1, D-70569 Stuttgart, Germany. Tel.: +49 711 689 1638.
E-mail address: m.ternes@fkf.mpg.de (M. Ternes).

doi:10.1016/j.progsurf.2009.09.001

1. Introduction

The control of the geometric, electronic, and magnetic properties of ordered structures at the nanoscale is necessary for the understanding and the fabrication of new materials and devices with structures as small as single atoms or molecules. In principle, there are two routes that lead to the construction of such ordered structures: (i) the “top-down” approach, which is an extension of current methods of microelectronic production, such as photolithography [1]; (ii) the “bottom-up” approach, where single atoms or molecules are manipulated using the sharp tip of a scanning tunneling microscope (STM) or atomic force microscope to create complex structures [2–7], or, alternatively, where atomic or molecular patterns are formed owing to the interaction between the constituents (self-assembly) or to a substrate template [8–12].

Here we discuss the formation of atomic superlattices formed by self-assembly owing to long-range indirect interactions mediated by substrate electrons. These interaction energies are very small and have to compare favorably with the other energies at play; therefore specific conditions are required for the formation and the observation of these superlattices.

The paper is organized as follows. In Section 2 we review how individual adsorbates modify the surface state and how this modification induces indirect interactions between pairs of adsorbates and leads to non-random distributions. Section 3 discusses in detail the properties of atomic superlattices. In particular, we focus on how the formation of hexagonal ordered superlattices takes place (Section 3.1), how this new superstructure modifies the surface state electrons (Section 3.3), and how melting occurs in these two-dimensional (2D) superlattices (Section 3.4).

2. Surface-state-mediated interactions between adatoms

Depending on the mutual distance r, the interaction between two adsorbed atoms or molecules can be classified as follows [13–19]: Owing to their exponential decay, direct electronic interaction and chemical bonds dominate only at very short distances. At larger separation, the interactions are prevalently indirect, i.e. mediated by the substrate, and can have different origins: charge transfer between the adsorbate and the surface induces a local dipole moment at the adsorbate which is the origin of repulsive electrostatic dipole–dipole interaction [20]. Mechanical stress induced in the surface by the adsorbate lead to local elastic deformations which for identical adsorbates result into a phonon mediated repulsive interaction [14]. Both of these interactions are decaying as $1/r^3$.

Furthermore, the adsorbate can be screened by substrate electrons with a decay proportional to $1/r^5$ for bulk electrons. In the special case of electronic indirect interactions mediated by surface electrons the decay is only $1/r^2$ [21]. These indirect interactions show oscillatory behavior in which the interplay between the two adsorbate alternate between attraction and repulsion.

A summary of the different types of adsorbate–adsorbate interactions is given in Table 1. In the following we will focus on indirect interactions between adatoms mediated by substrate electrons, specifically in the presence of a partially filled surface state band.

Table 1
Possible interactions, character, and decay behavior as a function of distance between two adsorbates. Here, r_0 is the characteristic decay length of the tail of the direct electronic interaction and corresponds to the decay of the participating orbitals and k_F the reciprocal wave vector of the participating electrons at the Fermi energy.

Interaction origin	Character	Decay
Direct electronic interaction	Attractive	$\exp(-r/r_0)$
Dipole-dipole interaction	Repulsive	r^{-3}
Strain induced interaction	Repulsive	r^{-3}
Indirect interactions mediated by bulk electrons	Oscillatory	$\cos(2k_F r)/r^5$
Indirect interactions mediated by surface state electrons	Oscillatory	$\cos(2k_F r)/r^2$

2.1. Early predictions and observations

Substrate electrons occupying bands near the surface are at the origin of indirect interactions between adsorbed atoms or molecules, as first suggested by Koutecky about 50 years ago [22]. In a way similar to the one described by Friedel for the screening of bulk impurities [23], the adsorbed species play the role of scatterers for the substrate electrons, giving rise to electronic density oscillations. These variations generate an oscillatory – attractive and repulsive – potential between the adsorbed species, with a characteristic periodicity corresponding to the electron wave vector at the Fermi energy. Subsequently, Grimley described theoretically the characteristics of this long-range indirect interaction [24,25]. Lau and Kohn showed that for interactions between adsorbates on a surface with a partially filled surface state band the interaction energy decays only with $1/r^2$ instead of $1/r^5$ as for interactions mediated by bulk states [21]. This result is obtained by considering an isotropic Fermi surface and applies to simple metals, while a more general approach is required in the case of metals with a complex Fermi surface [26].

The influence of indirect interactions on the distribution of adatoms on a substrate has been experimentally observed for the first time for adatoms on a transition metal by field-ion microscopy [27]. Later, indirect interactions have also been found in measurements resolving the reciprocal k-space as for example in low-energy electron diffraction [28] and ^{3}He spin-echo [29] experiments. In recent years the intriguing possibilities of the STM, i.e., its capability to atomically resolve surfaces and to probe locally the electronic structure, renewed the interest in the study of indirect adsorbate–adsorbate interactions. Several adsorbate-sample systems have been found in which long-range surface state mediated interactions between atoms, molecules, and clusters containing many atoms are the driving force behind structure formation.

2.2. The surface state of the (1 1 1) facets of noble metals

Noble metals as silver, gold, and copper have a face-centered-cubic (fcc) crystal structure. The hexagonal closed-packed (1 1 1) surface of these metals reveals three-fold symmetry, which can be made visible with STM as shown in Fig. 1b. The (1 1 1) surface of these metals is characterized also by the presence of a Shockley-like surface state [30,31] appearing at the Γ-point of the projected bulk band structure, with band edge E_0 below the Fermi energy. In the case of Ag(1 1 1) the band edge is at ≈ -63 meV [32–36]. The surface state electrons form a nearly free two-dimensional (2D) electron gas with an effective electron mass of $m^* = 0.42\,m_0$ (m_0: free electron mass) [32] and an almost parabolic energy momentum relation for low energies ($E \lesssim 250$ meV), as it can be described by the expression

$$E(\vec{k}) = \frac{\hbar^2 \vec{k}^2}{2m^*} - E_0 \qquad (1)$$

and schematically represented in Fig. 2a.

Scanning tunneling spectroscopy (STS) measurements reflect the local density of states (LDOS) [37,38]. For STS measurements the tip-sample separation is held constant and the tunneling voltage V_T is modulated by a small sinusoidal voltage (V_m). Then, V_T is ramped along the desired energy range and the differential conductance dI/dV is recorded with lock-in technique.

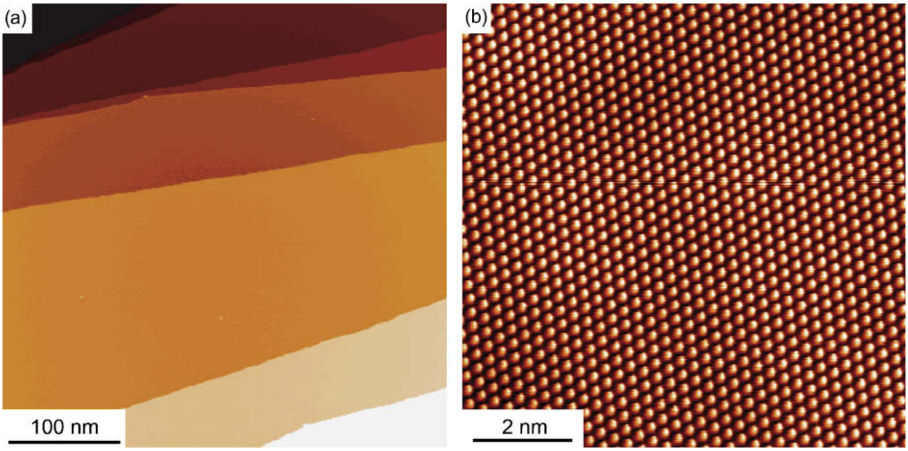

Fig. 1. STM measurements on a clean Ag(1 1 1) surface. (a) Overview image showing different terraces separated by monoatomic steps ($V_T = 20$ mV, $I_T = 20$ pA). (b) Atomically resolved image with characteristic threefold symmetry: the distance between neighboring atoms is 0.289 nm ($V_T = -30$ mV, $I_T = 0.3$ nA).

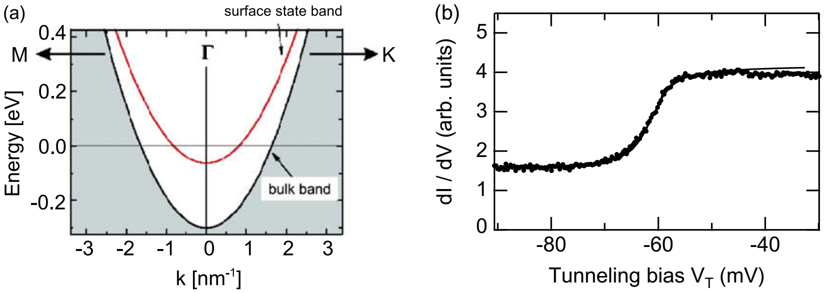

Fig. 2. Surface state on Ag(1 1 1). (a) Schematic representation of the projected band structure of the Ag(1 1 1) surface around the Γ point plotted in direction of the M and K point. The parabolic curve (red) describes the dispersion of the surface state. (b) Surface state as measured by dI/dV STS spectroscopy on a clean Ag(1 1 1) terrace (adapted from [35]). (For interpretation of the references to colour in this figure legend, the reader is referred to the web version of this article.)

On clean Ag(1 1 1) terraces, a step-like increase in dI/dV at $E_0 = -63$ meV can be observed, as expected for the electronic density of states (DOS) of a 2D system and shown in Fig. 2b. The lifetime of this state can be determined by the width Γ of the onset measured on large defect-free terraces. It yields a width of $\Gamma = 4.9$ meV corresponding to a surface-state lifetime $\tau = \hbar/\Gamma = 54$ fs [33,39,34,35].

Furthermore, mapping the LDOS at different tunneling voltages $eV_T > E_0$ close to surface steps or impurities allows the direct measurement of the energy-momentum relation corresponding to the parabolic dispersion of Fig. 2a [40]. The electron waves are reflected at steps and impurities producing an oscillating interference pattern (Fig. 3). Since these interference patterns are oscillations in $|\psi(\vec{r})|^2$ with $\psi(\vec{r})$ as the surface state electron eigenfunction, the spatial frequency of the pattern is given by $2k(E)$ with $k(E)$ as the inverse of the dispersion $E(k)$ of Eq. (1). This method has been successfully applied to measure the dispersion relation of the surface state of different metal surfaces [41–43,32,39].

2.3. Electron density oscillations

As shown in Fig. 3, impurities and adsorbates on the Ag(1 1 1) surface act as scatterers for the electron waves. They break the symmetry of a clean surface by inducing an additional local potential to the periodic potential of the surface atoms. The electrons around this perturbation attempt to screen

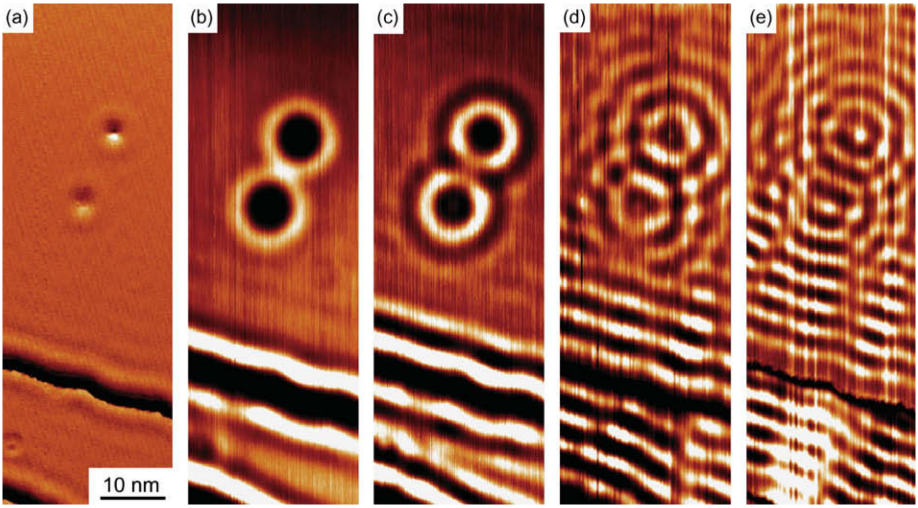

Fig. 3. dI/dV maps measured on Ag(1 1 1). (a) Topography image in second derivative shows three terraces separated by monoatomic steps ($V_T = -50$ mV, $I_T = 0.55$ nA). (b–e) dI/dV maps acquired at (b) $V_T = -50$ mV, (c) $V_T = -40$ mV, (d) $V_T = -20$ mV, (e) $V_T = +20$ mV. LDOS oscillations with an energy dependent wavelength, perpendicular to the step edge and surrounding the two impurities are visible.

the potential by density oscillations, so called Friedel-oscillations after Friedel who first described this kind of phenomenon theoretically [23]. The periodicity of this oscillation at the Fermi energy E_F is thereby determined by half of the wavelength $\lambda_F = 2\pi/k_F$ of the screening electrons [31].

In silver, the Thomas-Fermi wave vector for bulk electrons ($k_{TF} = 12\ \text{nm}^{-1}$) [44] is relatively large compared to that of the (1 1 1) surface state electrons of $k_F = \sqrt{2m^* E_0}/\hbar = 0.82\ \text{nm}^{-1}$. The short wavevector of the surface state electrons produces a 15-times larger oscillation wavelength, which makes the observation in STM much easier. Furthermore, the screening amplitude decays in the bulk with r^{-2}, while it decays on the surface for surface state electrons only with r^{-1} due to the dimensional restriction in two dimension [21].

A single Ce atom observed on a clean Ag(1 1 1) surface reveals this Friedel-like oscillatory modulation of the surface state electron density, as shown in Fig. 4a. The pseudo 3D representation results from a constant current STM image which was measured at a base temperature of $T = 3.9$ K to ensure that the Ce adatom is immobile during the measurement [45]. Concentric rings around the atom are clearly visible in the center of the image. The tunneling voltage V_T was set to -3 mV, very close to E_F, so that only the small interval between -3 mV and E_F of the LDOS contributes to the tunneling current and thus, the topographic image reflects mainly the LDOS at E_F. A first maximum exists at a radius of $\approx$3.2 nm from the center of the adatom, while the following rings are at a distance of $\lambda_F/2 \approx 3.8$ nm from each other, with λ_F as the in-surface Fermi-wavelength $\lambda_F = 2\pi/k_F$. The deviations from a perfect circular shape are due to interferences with reflections from other adatoms located farther away and therefore not seen in the figure.

For the LDOS at E_F, the variation can be described as the sum of the amplitude of an incoming and a reflected electron wave [41]:

$$\Delta\rho(r) \propto \frac{1}{k_F r}\left(\cos^2\left(k_F r - \frac{\pi}{4} + \theta_0\right) - \cos^2\left(k_F r - \frac{\pi}{4}\right)\right). \tag{2}$$

The phase shift θ_0 of the scattered wave reflects the interaction with the adsorbate. Simulating Eq. (2) and comparing it with the measured pattern results in a phase shift for Ce on Ag(1 1 1) of $\theta_0 = (0.37 \pm 0.05)\pi$ [45], as shown in Fig. 4b. The simulation is in good agreement with the results of Fig. 4a, except for the shape of the atom in the center of the image which is not included in the simulation.

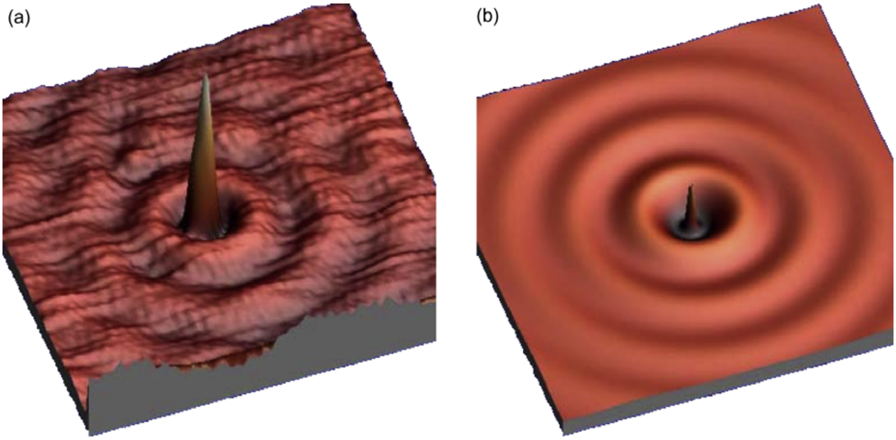

Fig. 4. (a): Friedel oscillation of a single Ce adatom on a clean Ag(1 1 1) surface observed at a base temperature of $T = 3.9$ K, a tunneling voltage of $V_T = -3$ mV, and a setpoint current $I_T = 20$ pA. Image size: 25×25 nm^2. (b) Simulation using Eq. (2) with a scattering phase shift of $\theta_0 = 0.37\pi$ and a wave vector at E_F of $k = 0.82$ nm^{-1}.

2.4. Non-random adatom distributions

A description of the indirect interaction mediated by surface-state electrons of Shockley surface states of (1 1 1) noble metal surfaces has been developed by Hyldgaard and Persson [46]. Their approach to describe the pair interaction between adsorbed species is especially adapted for the comparison with STM results. In the limit of large separations, the long-range oscillatory interaction is described by:

$$\Delta E_{pair}(r) \simeq -E_0 \left(\frac{2\sin(\delta_0)}{\pi}\right)^2 \times \frac{\sin(2k_F r + 2\delta_0)}{(k_F r)^2}, \tag{3}$$

where r is the distance between the adsorbates, E_0 is the surface state band edge onset energy with respect to the Fermi level E_F and k_F is the associated surface Fermi wave vector. δ_0 is the phase shift which describes the scattering properties of the adatom.

The first STM observation of the influence of surface-state long-range interactions has been reported for adatoms (S impurities) on Cu(1 1 1) [47]. Preferential distances in a range up to 10 nm corresponding to maxima in the measured surface LDOS, i.e., minima in the interaction potential, were observed. A more quantitative analysis was performed for Cu on Cu(1 1 1) [48], demonstrating the oscillatory behavior of the long-range interaction directly related to the LDOS variations observed by STM and the asymptotic decay $\sim 1/r^2$.

A more complete picture of the surface-state mediated interactions resulted from the comparison between three systems: Cu/Cu(1 1 1), Co/Cu(1 1 1), and Co/Ag(1 1 1) [49]. For these systems preferential distances between the adatoms are clearly found. A careful analysis of the experimental data demonstrated a good agreement with the theoretical model of Hyldgaard and Persson. The influence of the nature of the substrate (Cu vs. Ag), corresponding to a difference in the surface state characteristics inducing a larger periodicity of the long-range interaction for Ag than for Cu and an interaction energy smaller for Ag than for Cu, was discussed. Furthermore, the scattering phase shift δ_0 changes between the two different substrates from $\frac{1}{2}\pi$ for Co on Cu(1 1 1) to $\frac{1}{3}\pi$ for Co on Ag(1 1 1)which was attributed to the difference in the electron density of the surface state [49]. Surprisingly the adsorbate nature (Cu vs. Co) on the same surface (Cu(1 1 1)) has no effect on the scattering phase shift and the interaction energy even though their diffusion barriers differ substantially.

Let us now turn to the influence of the surface-state mediated interactions for the system Ce on Ag(1 1 1) [50]. Fig. 5a shows a STM image, acquired at 3.9 K, of a Ag(1 1 1) surface with approximately

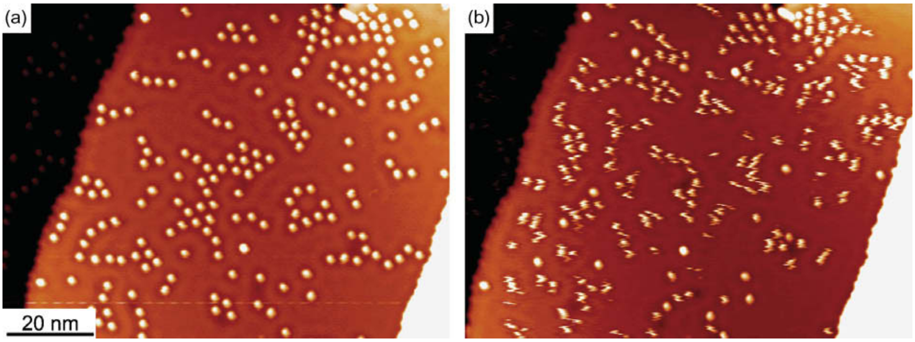

Fig. 5. (a) STM constant-current image of the Ag(1 1 1) surface covered by approximately 0.2% of a ML of Ce obtained at a temperature of 3.9 K ($V_T = -100$ mV, $I_T = 20$ pA). The Ce adatoms have a preferred next-neighbor distance of 3.2 nm. (b) STM constant-current image as in (a) but at a temperature of 4.7 K. The Ce adatoms are mobile and appear "fuzzy" while some dimers which have been formed are immobile (adapted from [50]).

0.2% of a monatomic layer (ML)[1] of Ce adatoms, deposited at ≈8 K. The tunneling voltage $V_T = -100$ mV and current setpoint $I_T = 20$ pA lead to a high tunneling resistance to prevent influences of the tip on the adatoms. The adatoms form chains and small islands with a typical adatom–adatom separation of 3.2 ± 0.05 nm.

After having increased the sample temperature to 4.7 K, the Ce adatoms look "fuzzy" due to the jumps of the adatoms to equivalent adjacent lattice positions on the underlying Ag(1 1 1) lattice, as visible in Fig. 5b. The few stable objects which remain immobile in the image are identified as dimers formed shortly after the Ce evaporation on the sample at a temperature of about 8 K. Even at the low setpoint current ($I_T = 20$ pA), some of the Ce adatoms show tip-induced motion. The atoms move in the direction of the scan as seen in multiple imaging of the same atom in several subsequent scan lines.

The observed average adatom–adatom distance of 3.2 nm matches the first maximum in real space of the electron density oscillation at E_F around a single Ce adatom, as seen in Fig. 4. The explicit theoretical analysis based on the Harris functional expression [51] was performed by Hyldgaard and Persson [46]. Their results lead to the following surface state mediated interaction energy between two adatoms:

$$\Delta E_{pair}(r) \simeq -E_0\left(\frac{(R-1)^2}{4} + R\sin^2(\delta_0')\right) \times \left(\frac{2}{\pi}\right)^2 \frac{\sin(2k_F r + 2\theta_0)}{(k_F r)^2}. \tag{4}$$

The interaction energy depends on the distance r between the adsorbates, the reflectivity R, the surface state band edge onset energy E_0 with respect to E_F, and the associated surface Fermi wavevector k_F. In addition to Eq. (3), scattering into bulk states is taken into account by a complex phase shift: $\delta_0 = \delta_0' + i\delta_0''$. With this definition, the reflectivity is given by $R = \exp[-2\delta_0'']$ and the Friedel-like phase shift at E_F for an isolated adsorbate can be written [46]:

$$\theta_0 = \tan^{-1}\left(\frac{1 - R\cos(2\delta_0')}{R\delta_0'}\right). \tag{5}$$

Using the observed phase shift $\theta_0 = (0.37 \pm 0.05)\pi$ (see Fig. 4), Eq. (4) has its first minimum at $r = 3.2 \pm 0.2$ nm and a weak local maximum at $r = 5.2 \pm 0.2$ nm (Fig. 6). The amplitude of the interaction energy depends therefore on the reflectivity R which can only be between 0.40 and 1.0 due to the restrictions implied by Eq. (5). For $R = 1$ the Ce adatoms act as perfect scatterers, i.e. no surface state electron waves are scattered into bulk states, and the trapping barrier for an adjacent adatom

---

[1] In the context described here, a monatomic layer of Ce means the complete coverage of the Ag(1 1 1) surface with Ce atoms having the same spacing as in their crystal lattice ($\approx 4 \times 10^{14}$ cm^{-2}).

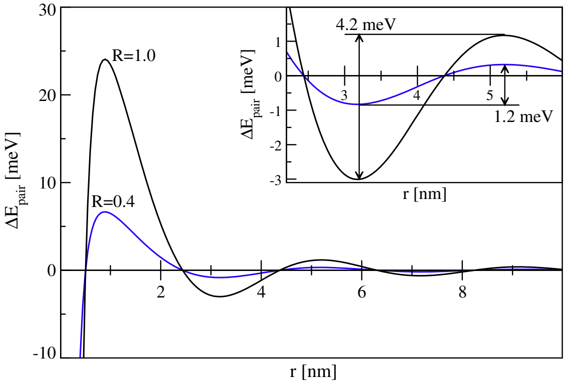

Fig. 6. Calculated surface state mediated interaction energy between two Ce adatoms on Ag(1 1 1) for $\theta_0 = 0.37\pi$ (full lines). Depending on the reflectivity R the trapping barrier for an adatom–adatom distance of 3.2 nm is between 1.2 – 4.2 meV.

at the position of minimal energy ($r = 3.2$ nm) is about 4.2 meV, while for $R = 0.4$ the trapping barrier decreases to about 1.2 meV.

As pointed out in Section 2, surface-state mediated interactions are not the only interactions at play. Single atoms on surfaces can be fully or partly ionized. The charge transfer between an adatom and the surface stems from the difference between the work function of the surface and the ionization energy of the adatom. This charge, together with the induced image charge in the metal, creates a dipole with moment of magnitude $p = 2dq$, where $2d$ is the distance between the adatom charge q and the image charge. The dipole–dipole interaction energy between two adatoms is repulsive and decays as [20]:

$$\Delta E_{p-p}(r) = \frac{p^2}{4\pi\epsilon_0|r|^3}. \tag{6}$$

The strength of the dipole can be determined for example by measuring the change of the work function between a pristine and a partly covered surface [53,54], or directly from adsorption distance and amount of the charge transferred [55]. As data concerning the dipole moment of Ce adatoms on Ag(1 1 1) are not available, an evaluation of the dipole–dipole interaction cannot be obtained. However, the formation of chains and small islands with preferred nearest-neighbor distance of 3.2 nm for low Ce coverage (see Fig. 5) demonstrates that the dipole–dipole repulsive interaction is negligible with respect to the surface-state mediated one, at least in this range of distances. Furthermore, for Ce on both Ag(1 1 1) and Cu(1 1 1), the dipole-dipole repulsion is weak enough to allow the formation of dimers, as visible for example in Figs. 9a and 20a. Therefore, for Ce on Ag(1 1 1) the dipole–dipole interaction will be neglected in the following. However, for other adsorbate-sample systems with larger dipole moment, as for example Cs/Ag(1 1 1) [54] and Na/Cu(1 1 1) (see Fig. 11), the dipole–dipole interaction plays a crucial role in the formation of the superlattice.

It is important to notice that the substrate temperature during the evaporation of the adsorbates is a critical parameter. This temperature has to be (i) high enough to permit diffusion for the adatoms to find the minimum of the surface-state mediated potential and (ii) low enough to avoid the formation of compact islands. These requirements define a narrow temperature range, which depends on the nature of both substrate and adatoms, for the indirect interaction to have an effect on the adatom distribution. The depth of the surface-state mediated attractive potential has to be compared with the diffusion barrier E_{diff} and to the repulsive potential close to the adatoms. Notice that typical diffusion barrier heights are one order of magnitude larger than the observed indirect interaction energies.

In addition to the theoretical modeling described in [46,56], *ab initio* studies of the influence of the indirect interactions have been performed. Some of them focussed mainly on the short-range part of the interaction, leading to results important for the interpretation of diffusion and nucleation [17,16,19]. The first *ab initio* calculation on the long-range tail of the surface-state mediated interactions was performed for Co adatoms on Cu(1 1 1) [57]. These results agree with the experimentally observed behavior for Co/Cu(1 1 1). An interesting finding is the preferential formation of adatom chains with adatoms at the distance corresponding to the first minimum in the interaction potential, instead of the development of 2D islands. This trend was already pointed out in Ref. [49] and attributed to the specific scattering properties of Co on Cu(1 1 1), i.e., to a scattering phase penalizing the distance corresponding to second-nearest neighbors in a hexagonal lattice. Subsequently, the effect of both, adatom concentration and substrate temperature on the formation of 1D chains vs. 2D islands has been investigated by kinetic Monte-Carlo (kMC) simulations for Co on Cu(1 1 1), Ce on Ag(1 1 1) [58], for Cu on Cu(1 1 1) [59], and for Fe on Cu(1 1 1) [60].

Furthermore, surface-state mediated interactions influence the distribution of single CO molecules adsorbed on Ag(1 1 1) where they preferentially adsorb near the minima of the surface state standing wave pattern [61]. Also Br adatom islands on Cu(1 1 1) have been found to favor spacings of half-multiples of the Cu(1 1 1) Fermi wavelength even at temperatures of 600 K [62]. The strong interaction potential which was found to be about 100 times higher than in the above mentioned systems and the decay length of the inter-island interactions were discussed in terms of multiple scattering sites along the edges of the islands and the highly electronegative Br acting as a strong scatterer. Furthermore, Ni adatoms on Ni ad-islands on Rh(1 1 1) form equilateral triangular clusters with 4–6 atoms per side and at room temperature [63]. Here, presumably strain favors the empty triangular shape instead of a hexagonal ordered lattice.

3. Adatom superlattices

An important implication and possible application of the long-range indirect interaction was pointed out in Ref. [49]: This interaction may lead to the formation of adsorbate superlattices, i.e., quasi-2D solids with a lattice parameter corresponding to the first minimum in the interaction potential. A crucial parameter is the adsorbate scattering phase shift, which determines the difference between the first minimum and the periodicity of the interaction ($\lambda_F/2$) at long-range. Depending on this phase, the second-nearest neighbor position can correspond to a repulsive region, hindering the formation of a 2D superstructure, or to a neutral position where the superlattice formation is not disturbed [49,11]. Nevertheless, we want to note that due to the $1/r^2$ decay in the pair-interaction (Eq. (4)), the next-neighbor attractive energy is always larger than the second-nearest neighbor repulsive energy. Thus, independent of the phase shift at the adsorbate location, hexagonal order can evolve when the adsorbate concentration, temperature, and diffusion barrier are tuned.

3.1. Formation of an adatom superlattice: Ce/Ag(1 1 1)

Cerium on Ag(1 1 1) was the first adsorbate-sample system where such a surface-state mediated 2D superlattice was observed [45]. A coverage of about 1% of a ML of Ce on Ag(1 1 1) leads to the formation of an ordered hexagonal arrangement of adatoms as shown in Fig. 7. The Ce adatoms are visible as bright spots forming a hexagonal superlattice, as confirmed by the Fourier transformation shown in the inset, with a distance between two neighboring adatoms of 3.2 ± 0.2 nm. This self-organized superlattice covers the entire Ag(1 1 1) surface up to macroscopic distances, i.e. taking images at different regions of the sample by displacing the tip in the millimeter range leads to the same superstructure [45].

To describe the interaction between the Ce adatoms in the lattice, we calculate the interaction energy for an adatom located at $\vec{r}$ surrounded by six neighbors at $\vec{r}_i (i = 1 \ldots 6)$ in hexagonal arrangement with an adatom–adatom distance of 3.2 nm. Using the pair interaction energy and an additional term for the interactions between three adsorbates [56] results in an interaction energy for the central atom of:

$$\Delta E_{int}(\vec{r}) \simeq \sum_{i=1}^{6} \Delta E_{pair}(|\vec{r}_i - \vec{r}|) + \sum_{i=1}^{6} \sum_{j>i}^{6} \Delta E_{triple}(\vec{r}_i, \vec{r}_j, \vec{r}) \qquad (7)$$

with ΔE_{pair} as defined in Eq. (4), and

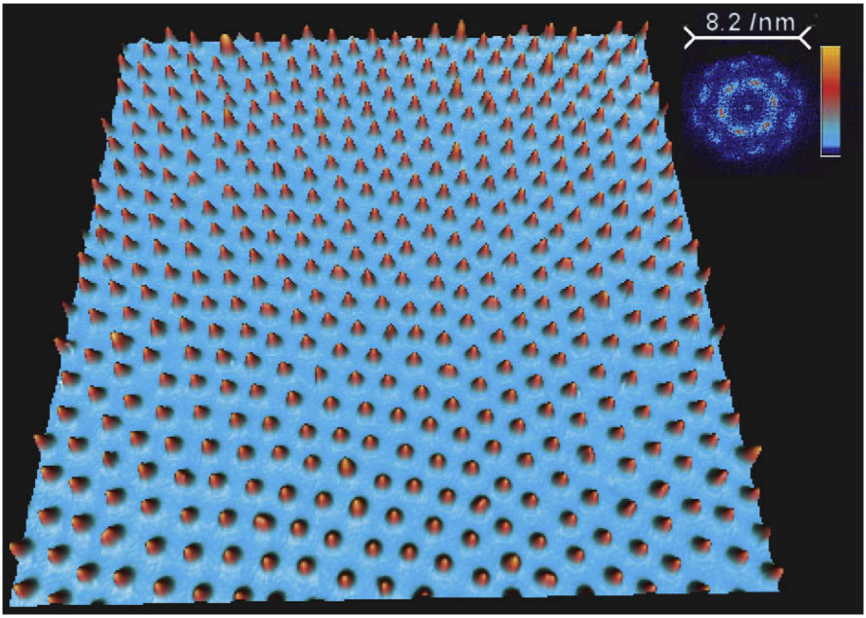

Fig. 7. Three-dimensional STM image of the superlattice of Ce adatoms on Ag(1 1 1) ($64 \times 64\ \text{nm}^2,\ V_T = -100\ \text{mV},\ I_T = 10\ \text{pA}$). Inset: Fourier transform of the STM image confirming the hexagonal structure of the superlattice (adapted from [45]).

$$\Delta E_{triple}(\vec{r}_i, \vec{r}_j, \vec{r}) \simeq -E_0\left(\frac{(R-1)^2}{4} + R\sin^2(\delta_0')\right)^{3/2}\left(\frac{16\sqrt{2}}{\pi^{5/2}}\right)\gamma_{123} \times \frac{\sin(2k_F r_{123} + 3\theta_0 - 3\pi/4)}{(k_F r_{123})^{5/2}} \tag{8}$$

with the definition of θ_0 as in Eq. (5) and

$$r_{123} = |\vec{r}_i - \vec{r}_j| + |\vec{r}_i - \vec{r}| + |\vec{r}_j - \vec{r}| \quad \text{and} \quad \gamma_{123} = 2\left(2\frac{r_{123}^{3/2}}{\sqrt{|\vec{r}_i - \vec{r}_j||\vec{r}_i - \vec{r}||\vec{r}_j - \vec{r}|}}\right).$$

Minimizing the interaction energy ΔE_{int} by varying the adatom–adatom distance d with a constant phase shift set to $\theta_0 = (0.37 \pm 0.05)\pi$ results in $d = 3.2 \pm 0.2$ nm, which is in excellent agreement with the observed one.[2] The corresponding energy map coded in gray levels (dark: low values, bright: high values) and a cross section is shown in Fig. 8.

Depending on the reflectivity R, the central atom resides in an energetic minimum ($\vec{r} = \vec{0}$) induced by the six next-neighbor Ce adatoms and gains an energy between 6.7 meV (for $R = 0.43$) and 31 meV (for $R = 1$) with respect to the energy at infinite position ($|\vec{r}| \to \pm\infty$). The formation of dimers is inhibited by the potential wall at $|\vec{r}| \approx 2.3$ nm. Furthermore, Fig. 8 exhibits an almost parabolic energy-position relation for small variations of $\vec{r}$ around the most stable position at $\vec{r} = \vec{0}$.

Fig. 9a shows a close-up view of a region of the Ce adatom superlattice at 3.9 K. The adatoms and few dimers, recognizable from their elongated shape, are immobile. In Fig. 9b the same region of the superlattice is measured at 4.8 K: at this temperature only the dimers stay at fixed position, while the Ce atoms diffuse between lattice sites around their equilibrium position.

Using the statistical distribution of the variation of the adatom position between two successive scan lines at a temperature of $T = 4.8$ K, which occurs due to random jumps of the Ce adatom from

---

[2] Higher order processes, i.e. interactions between 4 or more atoms have very small influence on the overall energy due to the rapid spatial decay of the wave-functions and are neglected.

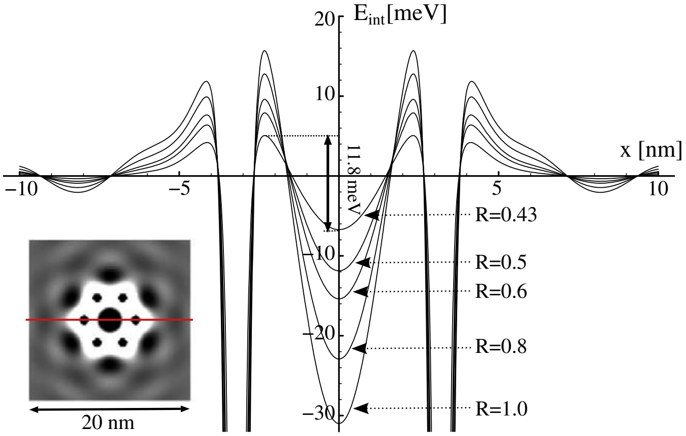

Fig. 8. Calculated potential landscape and cross-section along the direction $\vec{r} = \begin{pmatrix} x \\ 0 \end{pmatrix}$ (red line) of the pair- and three-adsorbate interactions for a single adatom surrounded by 6 in hexagonal order fixed adatoms (small black spots in the intensity plot) with an adatom–adatom distance of 3.2 nm and different coefficients R. For the reflectivity $R = 0.43$ the confining potential is given by 11.8 meV. (For interpretation of the references to colour in this figure legend, the reader is referred to the web version of this article.)

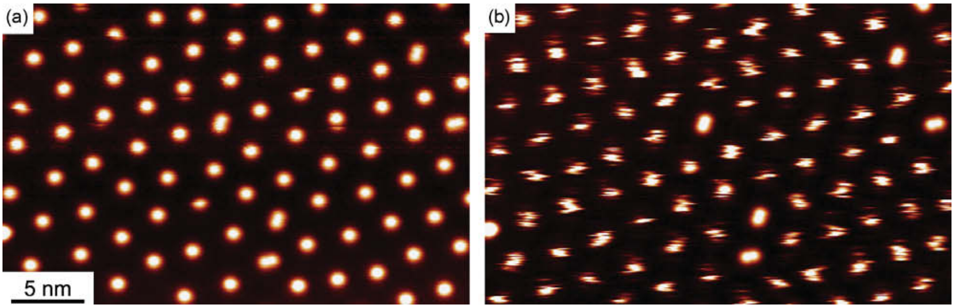

Fig. 9. Constant-current STM images of the Ag(1 1 1) surface covered by approximately 1% of a ML of Ce obtained at a temperature of (a) 3.9 K and (b) 4.8 K with the same image-size of 35 × 22 nm^2($V_T = -100$ mV, $I_T = 20$ pA). At 3.9 K the Ce adatoms are immobile during the time of data acquisition, while they look "fuzzy" due to jumps between lattice-sites of the underlying Ag(1 1 1) surface during the scanning at the slightly elevated temperature of 4.8 K (adapted from [45]).

one atomic position to another within the well as seen in Fig. 9b, we determine directly the reflectivity R by comparing to the Boltzmann distribution

$$n(\vec{r}) = n_0 \exp\left[-\frac{\Delta E^R_{int}(\vec{r}) - \Delta E^R_{int}(\vec{0})}{k_B T}\right]. \tag{9}$$

The result is displayed in Fig. 10 and shows a Gaussian distribution with a full width at half maximum of 0.57 ± 0.02 nm, consistent with the approximately parabolic potential well. A least square fit of Eq. (9) to the data results in a reflectivity of $R = 0.43 \pm 0.01$ and thereby in a superlattice confining potential of 11.8 ± 1.2 meV (see Fig. 8).[3] The fact that we measure changes only in one direction of the distribution was taken into account in our analysis. It should approximate the true adatom distribution as

---

[3] The interplay between the phase shift θ_0 and the reflectivity R depends on the intrinsic binding of the Ce adatom to the Ag(1 1 1) surface. Since a high percentage of electrons are scattered into bulk states the adsorption seems to be dominated by the interaction with bulk states.

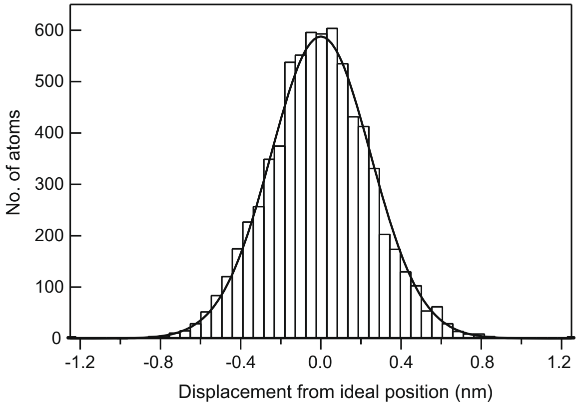

Fig. 10. Histogram of the measured Ce adatom displacement from the ideal position of the hexagonal superlattice sites at 4.8 K (bars) and statistical analysis using the $E_{int}(r)$ relation of Eq. (7) and the Boltzmann distribution. The best agreement is obtained for an adatom reflectivity of $R = 0.43$ (adapted from [45]).

long as $\tau_{tip} \ll \tau_{jump} \ll \tau_{atom}$, where $\tau_{tip} \simeq 30$ ms is the time to scan over a single adatom, τ_{jump} is the temperature dependent characteristic adatom hopping time from one Ag(1 1 1) lattice site to another, and $\tau_{atom} \simeq 16$ s is the total time during which a given adatom is monitored and hopping events can be recognized. The average time between two jumps $\tau_{jump} = 300 \pm 100$ ms is estimated from the statistical probability of observing a jump during τ_{tip} and the probability of observing no jumps during the time of 1 s between successive scans over a given adatom. Non-negligible possible forward–backward jumps due to $\tau_{jump} \ll 1$ s are thereby included.

Assuming an attempt frequency of $\nu_0 = 10^{12\pm0.5}$ Hz [49] we calculate the diffusion barrier for the Ce adatom on the Ag(1 1 1) lattice to

$$E_{diff} = k_B T \ln(\nu_0 \tau_{jump}) = 10.9 \pm 0.7 \text{ meV}. \tag{10}$$

Thus, reducing the base temperature to $T = 3.9$ K "freezes" the superlattice as seen in Fig. 9a because the adatom hopping time τ_{jump} increases to several minutes.

To summarize, at low Ce adatom concentration $\ll 1\%$ ML the interaction energy between two Ce adatoms creates only a shallow potential well of 1.2 meV (see Fig. 6), not enough to trap the adatom at $T = 4.8$ K and to form an ordered structure except for small regions with locally higher adatom concentrations as seen in Fig. 5b. At higher adatom concentration the superlattice is created because adatoms inside an ordered lattice are trapped in a sufficiently deep potential well of 11.8 meV.

The low diffusion barrier, which is of the same order of magnitude, allows the adatom to find the energetically preferred position in the superlattice. On the other hand, for systems which require higher temperatures owing to higher diffusion barriers to allow adatom diffusion (as for example Cu/Cu(1 1 1) [48] or Co/Ag(1 1 1) [49]) the long-range surface-state mediated interaction potential is too weak compared to the diffusion potential to create ordered structures on a larger scale.

This view is in agreement with kinetic Monte-Carlo simulations in these systems [58,64]. Using long-range interaction energies between the adatoms from ab-inito calculations [65], Negulyaev et al. showed that Co on Cu(1 1 1) as well as Ce on Ag(1 1 1) form linear chains at low adatom concentrations. The average length of these chains depends on the temperature. At elevated temperatures, i.e. increased kinetic energy of the adatoms, the trapping energy is too small to form longer chains [58].

Furthermore, at higher Ce concentration (1% ML) the initially (after evaporation) random distribution rearranges in the simulation to hexagonal ordered structures at a temperature of 4 K [64]. Increasing the temperature above ≈8 K leads to the irreversible collapse of the superlattice owing to the formation of immobile dimers in agreement with experiments [50].

3.2. Other adatom–substrate combinations

Since the first observation of the Ce/Ag(1 1 1) superlattice formation, other adsorbate–surface combinations, as for example Ce/Cu(1 1 1) [66,67], have been found to form a surface-state mediated superlattice. As one would expect from the above-developed models, the adatom spacing in this superlattice is smaller due to the reduced wavelength of the Cu(1 1 1) surface-state ($\lambda_F = 3.0$ nm [41]) at the Fermi energy. Thus, an amount of about 0.04 ML of Ce atoms is necessary to create a complete superlattice. The average adatom–adatom distance is then $d \approx 1.4$ nm, which is compatible with a scattering phase shift of $\theta_0 \approx 0.2\pi$. We note that for this phase shift the second-nearest neighbor position is not repulsive [49] which stablizes the superlattice.

Cs/Cu(1 1 1) [68] and Cs/Ag(1 1 1) [54] have been also found to form hexagonal superlattices. For these systems, however, the surface-state mediated interaction does not provide the only contribution to the superlattice self-assembly. A repulsive dipole–dipole interaction, characterized by a $1/r^3$ decay (see Eq. (6)), participates in the formation of the ordered Cs overlayer [69]. For Cs on Cu(1 1 1) [68] a hexagonal superlattice with a lattice parameter of 1.1 nm has been reported for the lowest investigated coverage of 5% ML. Although the phase shift for Cs can be different than for Ce, this coverage is already higher than the one leading to a surface-state mediated superstructure. This behavior is even more evident in the results for Cs on Ag(1 1 1) [54], where for a Cs coverage of 3–4% ML a superlattice with a nearest neighbor distance of 1.5 nm has been reported. For Ce on Ag, we have seen that the equilibrium distance is 3.2 nm, and that for coverage higher than 1.7% ML the Ce adatoms do not form any ordered superlattice [50], indicating that for Cs a different process takes place. These results can be understood by taking into account a dipole–dipole interaction between the charged Cs adatoms. This repulsive interaction plays an important role in preventing the formation of Cs dimers at the surface, even at higher coverage.

Furthermore, we have recently observed a superlattice of Na adatoms on Cu(1 1 1). For a coverage of ≈4% ML a well ordered superlattice with an interatomic distance $d \approx 1.5$ nm is formed, as shown in Fig. 11. The nearest-neighbor distance compares well with the one found for other surface-state mediated ordered structures on Cu(1 1 1) (Ce, Cu, Co). For this system, however, the absence of defects and dimers is remarkable. Therefore, also here, the electrostatic repulsive interaction contributes to the stabilization of this superlattice. Similar behavior has been reported for adsorbed molecules: for a dipolar iridium complex [70] and for tetrathiafulvalene molecules [71] an intermolecular long-range repulsive interaction is at the origin of the formation of a coverage-dependent superstructure.

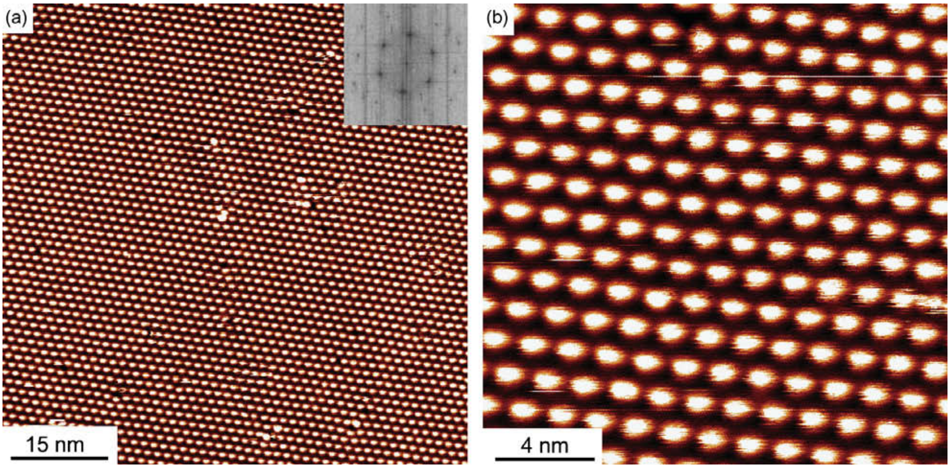

Fig. 11. Superlattice formed by Na/Cu(1 1 1). (a) Overview image ($V_T = 0.5$ V, $I_T = 10$ pA). The absence of defects or dimers is remarkable. Inset: Fourier transformation. (b) Detail image ($V_T = 0.5$ V, $I_T = 10$ pA), average nearest neighbor distance: 1.5 nm.

The prevention of dimer and cluster formation is important to obtain large, defect free superlattices. As shown for Na/Cu(1 1 1) (Fig. 11), Cs on Cu(1 1 1) [68] and on Ag(1 1 1) [54], electrostatic repulsion can impede the adatoms to form dimers. In a recent study of Fe adsorbates on Cu(1 1 1) an opposing driving force towards dimer formation has been found [72]. The next-neighbor distances of 1.2–1.5 nm found in this system agree with the attractive part of the surface-state mediated potential and hexagonal self-ordering was observed. Nevertheless, large-scale topographic images revealed that the formation of clusters inhibits the creation of a macroscopic-ordered Fe superstructure on Cu(1 1 1). The authors compared the experimental morphology with the results of kinetic Monte-Carlo simulations and found that the formation of clusters is promoted by the local strain of the substrate imposed by the Fe adsorbates [72]. This result seems to be in contradiction to the simple picture of repulsive strain induced interactions outlined in Section 2 and Table 1 but in this system the strain induces very locally an attractive potential which increases only slightly the capture radius for dimer and cluster formations. Similar behavior was found in other systems as for example embedded Co clusters in a Cu(0 0 1) surface [73].

Superlattices of 3d-metal adatoms are of considerable interest because their magnetic exchange interaction is expected to be of the same order of the surface-state mediated interaction energy [74]. Calculations performed on Cu(1 1 1) show that, for Ti, V, Cr, and Ni pairs, the magnetic coupling mediated by the surface-state electrons is ferromagnetic, while for Mn, Fe, and Co pairs antiferromagnetic states are more stable which, in a hexagonal nanostructure, can lead to magnetic frustration and noncollinear magnetic states [65].

Furthermore, an interesting approach to increase the exchange interaction between magnetic adatoms at large distances by artificially constructed quantum resonators was discussed [75]. Quantum corrals [76,3] and quantum mirrors build with the STM by the means of atom manipulation would act as additional reflectors for the surface state electrons. To prevent these structures to take part in the self-organization of the adsorbates immobile dimers could be used. For example, a 'quantum onion', the self-assembly of Ce adatoms into different concentric circular orbits inside a corral of Ce-dimer is feasible [77].

Two examples of the effect of surface-state mediated interactions in one dimensional systems have been reported. In the first one, the Ag(1 1 1) surface state is confined to one-dimensional nanogratings formed by self-assembled methionine molecules. Subsequent deposition of Co or Fe adatoms on the nanostructured surface shows a self-alignment of the adatoms in the nanogratings. This one-dimensional self-ordering is induced by the long-range interactions mediated by the Ag(1 1 1) surface-state electrons [78]. In the second example, Co adatoms are found to self-align on a Si(1 1 1)-(4×4)-In striped template. This self-assembly originates from the indirect interaction between Co adatoms mediated by a quasi-one dimensional electron gas confined to the In wires [79].

3.3. Interplay between superlattice stability, adatom density and substrate electronic structure

The creation of the highly ordered adatom superlattices on the Ag(1 1 1) and Cu(1 1 1) surface with its characteristic two-dimensional surface state is well described in the framework of long-range adatom–adatom interactions. But this model does not provide results for the electronic behavior of the surface state in interaction with the scattering pattern.

Thus, STS measurements were performed on the stable Ce/Ag(1 1 1) superlattice at a reduced base temperature of 3.3–3.9 K to prevent movements of the adatoms during data acquisition. Fig. 12a presents a close-up $(7.5 \times 7.5\ \mathrm{nm}^2)$ constant current STM image of the Ag(1 1 1) surface covered with approximately 1% ML Ce forming a well ordered hexagonal superlattice with an adatom–adatom distance of $d = 3.2$ nm. The dI/dV spectrum shown in Fig. 12c (black curve) was measured in the center of the triangle formed by three Ce adatoms as marked in Fig. 12a. Compared to the spectrum obtained on clean Ag(1 1 1) (blue curve), the spectum has changed dramatically. Instead of a step like increase in the differential conductance at the surface state band onset of -63 meV (see Fig. 2b), two relatively broad peaks are observed at approximately 85 and 210 meV. Using the energy of the first peak as the tunneling voltage for spectroscopic mapping of the differential conductance, the image in Fig. 12b is obtained, revealing a maximum in the LDOS in the center of the triangles, and a minimum centered on the Ce adatoms with a finite spatial extent.

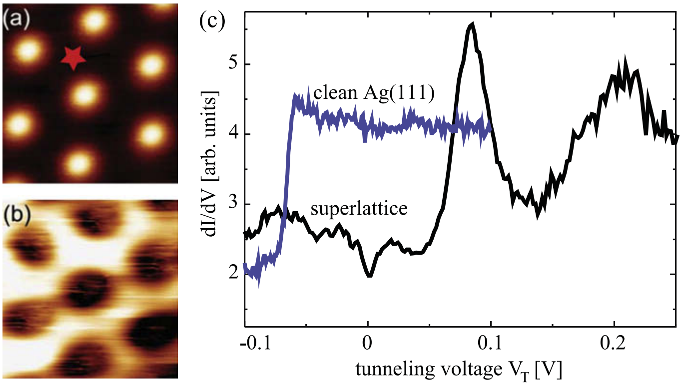

Fig. 12. (a) STM image of a hexagonal unit cell of the superlattice of Ce adatoms on Ag(1 1 1) with an adatom–adatom distance of $d = 3.2$nm (image size: 7.5×7.5 nm^2, $V_T = -100$ mV, $I_T = 10$pA). The red star marks the point where the spectrum (c) was measured. (b) dI/dV map of the same area at $V_T = 85$ mV, corresponding to the energy eV_T of the first peak of the spectrum. (c): dI/dV-measurement of the clean Ag(1 1 1) surface showing the unperturbed surface state (see Section 2.2) in blue (set point before opening the feedback-loop: $V_T = -100$ mV, $I_T = 1$ nA,$V_m = 5$ mV) and dI/dV measurement in the center of the triangle formed by Ce adatoms in black (average of 5 spectra, $V_T = -109$ mV, $I_T = 10$ pA,$V_m = 5$ mV) (adapted from [80]). (For interpretation of the references to colour in this figure legend, the reader is referred to the web version of this article.)

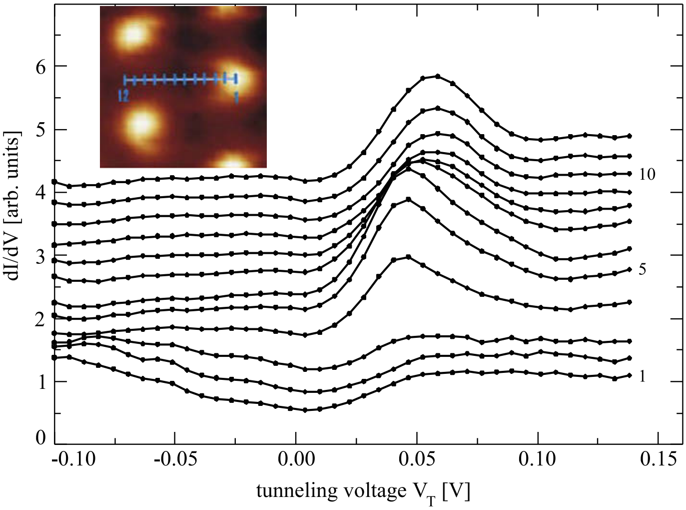

Fig. 13. Set of dI/dV spectra measured in a hexagonal superlattice with an adatom–adatom distance of $d = 3.5$ nm from an on top position (1–3) to a center position (4–6) and a bridge site (10–12). For illustration see the inset STM image where the positions are marked. The spectra are shifted vertically with respect to each other for better visualization. The set point before opening the feedback loop was for all spectra: $V_T = -100$ mV, $I_T = 19.5$ pA at $T = 3.3$ K and $V_m = 10$ mV.

Additional site-resolved spectroscopic measurements in a slightly larger superlattice at a Ce adatom concentration of approximately 0.7% ML resulting in a superlattice spacing of $d = 3.5$ nm were performed, showing structures in the spectra that strongly depend on the spatial position, as seen in Fig. 13. On top of the Ce adatoms (curves 1–3) the spectra are mainly flat with a broad gaplike structure between approximately -75 and +35 meV. When moving the tip away from the center of gravity of the adatom, a peak at an energy of approximately +45 meV arises which has its maximum intensity in the center position of the triangle formed by three Ce adatoms (curves 4–6). The position of the peak is shifted towards lower energies compared to the measurement in the $d = 3.2$ nm superlattice (Fig. 12c). Furthermore, at a bridge site position, i.e. in between two adatoms (curves 10–12), the intensity of the observed peak is slightly reduced and shifted to higher energies (approximately +60 meV).

To get an adequate overview of the spatial location and energy of the peaks in the LDOS, 1024 spectra were measured in a raster of 32×32 points covering completely one hexagon of the superlattice. Each spectrum therefore contains 24 data points measured at a tunneling voltage V_T between -100 and +130 mV. All the data points of the 1024 spectra that correspond to a certain energy were combined into a color-coded image (color scale: blue–red–yellow corresponding to low-medium-high dI/dV signal-strength) as presented in Fig. 14. The maps at low energies of -100 and -90 meV reveal a faint higher dI/dV signal on top of the adatoms as in the region between the adatoms. Between an energy of about -60 and +20 meV the maps show no difference in the dI/dV signal over the whole recorded area, while at energies $eV_T \geqslant 40$ meV a strong dI/dV signal with a maximum at about 60 meV occurs in the region between the adatoms.

The average distance d between two Ce adatoms in the superlattice depends on the Ce coverage, and was determined experimentally to be in the range of $d = 2.3$ nm (for $\approx$1.6% ML) to $d = 3.5$ nm (for $\approx$0.7% ML). Higher Ce coverages (> 1.7% ML) result in the formation of clusters [50] with no long-range order, while lower coverages (<0.7% ML) lead to the formation of islands of Ce adatom superlattices with the energetically most favored interatomic distance of $d = 3.2$ nm and empty areas in between. The position of the first peak in the spectra recorded at the center of a triangle formed by three Ce adatoms depend critically on the adatom–adatom distance d, as shown in Fig. 15 which compares the spectra taken in superlattices with five different average adatom distances. For higher Ce concentration, i.e. smaller d, the position of the first peak shifts quadratically to higher energies. Additionally, the peaks are broadened due to the increased disorder in compressed lattices ($d < 3.2$ nm).

To rationalize the observed spectral features we might apply a simple model assuming an undisturbed, infinite 2D superlattice of regularly arranged Ce adatoms on the Ag(1 1 1) surface with a fixed adatom–adatom distance of $d = 3.2$ nm and a perfect free-electron-like surface state with parabolic band dispersion as described by Eq. (1). This regular superlattice with its adatom–adatom distance of about 11 Ag lattice sites (the nearest neighbor distance of the Ag-atoms on the Ag(1 1 1) substrate is 0.289 nm) creates a new 2D-mini-Brillouin-zone which is very small compared to the bulk one.

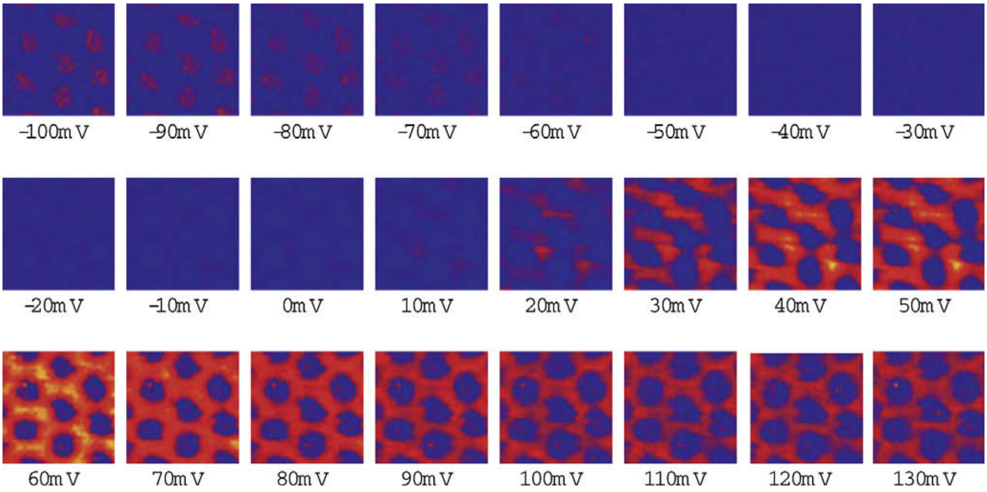

Fig. 14. Combined images of 1024 (32×32) spectra measured in a Ce adatom superlattice with an adatom–adatom distance of $d = 3.5$ nm at a base temperature of $T = 3.3$ K. Each image corresponds to the map of the dI/dV signal of the 1024 spectra at the marked tunneling voltage V_T coded in color (blue–red–yellow: low-medium-high signal strength). (For interpretation of the references to colour in this figure legend, the reader is referred to the web version of this article.)

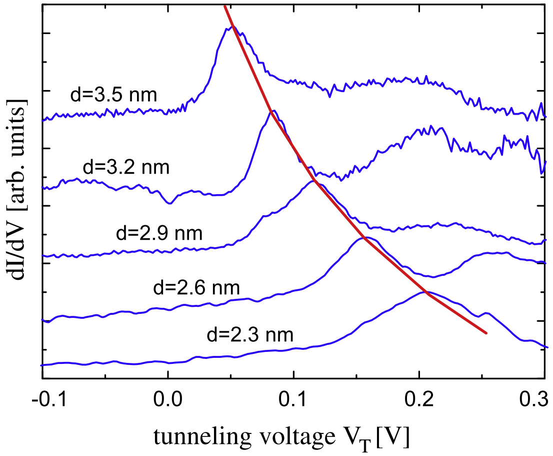

Fig. 15. Set of spectra taken in the center of a triangle formed by three Ce adatoms in a hexagonal superlattice. The adatom–adatom distance d decrease from the top to the bottom spectrum due to higher Ce coverage and thereby higher superlattice compression. The red line mark the shift of the first peak in the spectra from approx. 50 meV ($d = 3.5$ nm) to approx. 200 meV ($d = 2.3$ nm). The spectra are shifted vertically in respect to each other. (For interpretation of the references to colour in this figure legend, the reader is referred to the web version of this article.)

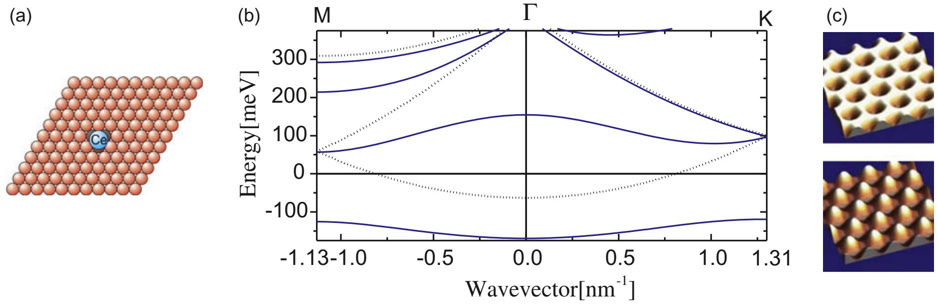

Fig. 16. (a) $l \times l$ unit cell used for the TB calculation. The Ce adatom interacts only with the three nearest Ag neighbors (dark spheres). (b) Band structure of the 2D system for $d = 3.2$ nm. Dotted lines: folded dispersion of the unperturbed free electron in the empty lattice approximation; solid lines: TB calculation showing the opening of a band gap between −120 meV and 60 meV. (c) In real space the occupied band is located at the adatom positions, while the unoccupied band is located interstitially (adapted from [80]).

Fig. 16b (dotted lines) shows the resulting folded band structure of the Ag(1 1 1) surface state along directions of high symmetry. The degeneracies at the K and M points correspond to energies of $E_M = 58$ meV and $E_K = 98$ meV, close to the observed peak in STS.

To obtain deeper insight into the physics of the superlattice creation and stabilization, tight-binding (TB) simulations have been performed [80]. First, the characteristics of the surface state as well as the observed Friedel-like oscillations in the presence of one Ce adatom, i.e., the phase shift (see Fig. 4), are reproduced by the TB model which fixes the hopping parameter the interaction potential between the Ce adsorbate and the three direct neighbors of the underlying Ag surface. Then, the superlattice is modeled by a hexagonal periodic arrangement of Ce adatoms adsorbed on Ag(1 1 1) hollow sites, as depicted in Fig. 16a. The band structure and the DOS of the superlattice are calculated as shown in Fig. 16b for a superlattice spacing of $d = 3.2$ nm.

At the high symmetry points K and M the lower band is shifted towards lower energies, while the upper band still lies at the energy of the empty lattice approximation. This asymmetric opening of an energy gap at the reduced-zone boundaries leads to peaks in the DOS due to band flattening. These peaks are also reflected in the LDOS, but with different amplitudes depending on the site in the unit cell. States in the lower (filled) band are concentrated close to the Ce adatoms, to take advantage of the attractive potential there, while states in the upper (empty) band are concentrated at positions between the Ce adatoms (see Fig. 16c).

In Fig. 17 the calculated LDOS at the center of a triangle formed by three Ce adatoms is compared to experimental results. The lowest band is between -170 and -120 meV, but its contribution to the LDOS calculated at that point is very small. Apart from the tunneling region below -100 mV, the agreement is remarkably good, especially considering the fact that this is not a fit but a prediction without adjusting the microscopic parameters of the model.

Using the same parameters in the TB model, but adjusting the size $l \times l$ of the supercell by taking for l the closest integer to d/a with $a = 0.289$ nm (the distance between two Ag atoms), the shift of the energy of the first peak for different superlattices is also very well reproduced by the TB calculation (see Fig. 18a). This shift varies linearly with the inverse area Ω^{-1} of the triangle formed by three adsorbates with an adatom–adatom distance d, so that the first peak is localized at an energy

$$E = E_0 + (620 \pm 10)\ \mathrm{meV\,nm}^2 \times \frac{1}{\Omega}. \tag{11}$$

This behavior can be easily understood within a model of confinement in a 2D box [81]. A triangle with perfectly reflecting walls would lead to a slope of $6\sqrt{3}\pi^2\hbar^2/m^* = 726$ meV $\times$ nm^2, while it is reduced in the Ce superlattices due to the phase shift during the scattering process of the electron waves at the adatoms.

The TB calculation allows one to understand why the superlattice has a "natural" periodicity of $d = 3.2$ nm. Indeed, the gap opening in the free Ag(1 1 1) band structure which is induced by the Ce potential increases the number of states below E_F and decreases their energy. Thus, it is useful to calculate the energy of the lowest band,

$$E_{\mathrm{band}} = \int_{-\infty}^{E_F} E \times n(E)dE \tag{12}$$

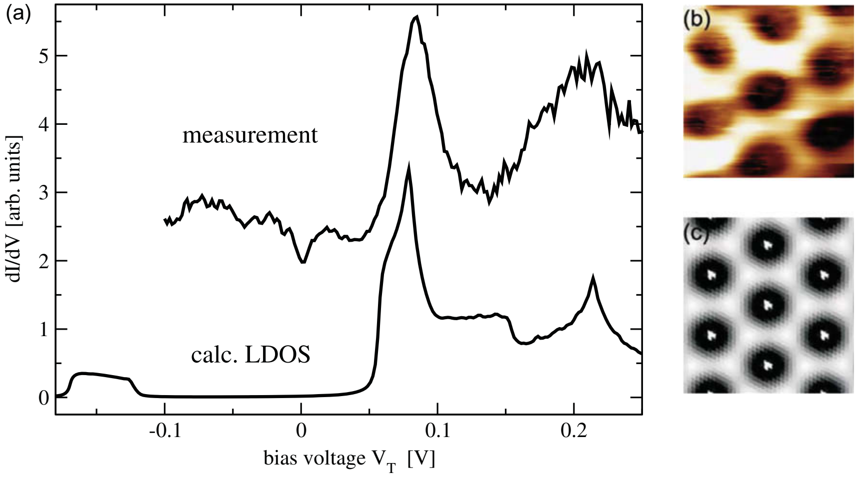

Fig. 17. (a) TB calculation of the LDOS and dI/dV measurement in the center of the triangle formed by Ce adatoms with an adatom spacing of $d = 3.2$ nm. The set point for the measurement before opening the feedback loop was $V_T = -109$ mV and $I_T = 5$ pA with a modulation voltage of $V_m = 2.5$ mV. The calculation, in contrast to the measurement, does not include the contribution of bulk states to the LDOS. (b) dI/dV-map at $V_T = 85$ mV. (c) TB calculation of the spatial LDOS at an energy of 85 meV (adapted from [80]).

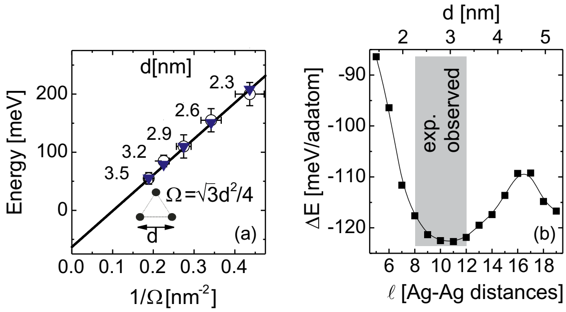

Fig. 18. (a) Energy of the maximum of the first peak in a spectrum measured in the center of a triangle formed by three Ce adatoms as a function of the inverse area Ω^{-1} of the triangle (circles: measurements; triangles: TB calculation). The larger error-bars for the experimental data for smaller adatom–adatom distances d are due to the fact that compressed lattices ($d < 3.2$ nm) spread the observed values (see also Fig. 15). (b) Energy difference ΔE between adsorbate-covered and clean surface per Ce adatom, calculated for each unit-cell size. The solid line serves as a guide for the eye. The gray area marks the range of the adatom–adatom distances where complete superlattice formation was found (adapted from [80]).

for the clean and for the Ce covered surface. The difference between both gives directly the contribution of the Ag surface state to the gain in energy per Ce adatom for each unit cell size $l \times l$ (see Fig. 18b). The most favorable configuration corresponds to a Ce–Ce distance of 3.2 nm, precisely the distance realized experimentally in most cases. The energy gain remains significant for Ce–Ce distances in the range $d = 2.3$—3.5 nm, the distances found as a function of Ce adatom concentration. This effect is analogous to charge-density wave (CDW) formation in correlated systems [82], but the potential that stabilizes the CDW here is external (the Ce atoms) while it is self-consistently induced by correlations in a standard CDW. The optimal Ce–Ce distance agrees with that predicted by Hyldgaard and Persson [46,56] as it was shown in Section 3.1. Note, however, that the dramatic effects of the superlattice on the surface state (gap openings, LDOS singularities) cannot be accounted for by the model of Hyldgaard and co-workers.

Furthermore, the model allows us to study the effect of local disorder on the LDOS with respect to a perfect periodic arrangement of Ce adatoms and to compare the calculation with the spectra obtained at different locations in a slightly disordered superlattice, as shown in Fig. 19a. The reproduction of the local environment around points A and B inside a 44×44 cluster of Ag atoms, which was then repeated periodically to minimize finite-size effects in the calculation is shown in Fig. 19b. To determine the degree of disorder in the local environment, the self-correlation is calculated as follows:

$$h(x,y) = \sum_{x'} \sum_{y'} I(x',y') \times I(x'+x, y'+y), \tag{13}$$

where $I(x,y)$ denotes the normalized z-height of the STM image at the position (x,y) [66]. For the results displayed in Fig. 19d we used for the summations a small area (± 7.5 nm) around the points $(x_0^{A(B)}, y_0^{A(B)})$ where the dI/dV spectra were taken. Any periodicity in the image will be shown as a periodic pattern, so that in a perfect superlattice with no disorder $h(x,y)$ would repeat the hexagonal order. As seen in Fig. 19d the ordering around point A is quite good up to three lattice distances, while around B a displacement of just two lattice distances smears out the result of the self-correlation function, indicating a much higher degree of disorder compared to the neighborhood of A.

The influence of the disorder on the dI/dV spectra is seen in Fig. 19c. The agreement between data and TB calculation is very good: The broadening and the shift of the main peaks are correctly reproduced except for a small shift in energy which might be due to a small systematic error in the determination of the exact adatom positions (calibration of the piezoscanner), as well as the position of the second peak at point A and its absence at point B. Remarkably, the shifts of the main peaks agree with Eq. (11) and Fig. 18a if d denotes the average distance between the 3 Ce adatoms in the triangular lattice that enclose the point A and B, respectively. Additionally, the absence of the second peak in B can be assigned to the higher degree of disorder. As seen in the TB band structure calculation (Fig. 16b), the

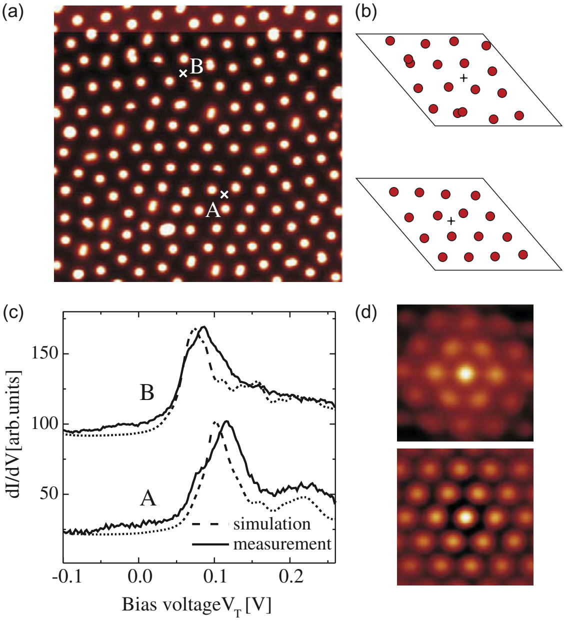

Fig. 19. (a) STM image of a slightly disordered system (35nm^2), $V_T = -100$ mV, $I_T = 10$ pA. (b) The local arrangement of Ce adatoms in a mesh of 44 × 44 Ag-atoms around the points *A* and *B* as used for the TB calculation. (c) Spectra obtained at the marked points *A* and *B* which differ by their nearest neighbor distances. The changes in peak position, intensity, and shape indicate the sensitivity of the electronic structure to local disorder. Dashed lines: TB calculation. For clarity the curves have been superimposed and curves *B* have been shifted vertically. (d) Self-correlation images of the area around *A* and *B* show that the region around *A* has a higher degree of order than the region around *B* (adapted from [80]).

second peak at about 200 meV is due to the flat band whose origin is in the second Brillouin zone. While the second closest adatom neighbors in *B* already show a sufficient amount of disorder, this band is already smeared out and therefore the formation of this peak is suppressed.

Directly over Ce adatoms the TB model predicts the onset of the lowest band below E_F. On measurements taken in the slightly expanded lattice with $d = 3.5$ nm a faint signal can be detected at $eV_T \approx -100$ mV on top of the Ce atoms which might be due to this band (see Figs. 13 and 14). The weakness or absence of contributions of this band can be understood by recalling that the tip is approximately 200 pm (i.e. the apparent height of one Ce adatom) further distant from the Ag(1 1 1) surface when placed above an adatom. Thus, the contribution of the disturbed surface state to the tunneling current is reduced.

3.4. Melting of superlattices

The first order phase transition which occurs when regular three-dimensional (3D) crystals melt and the highly ordered crystal structure changes into the irregular order of a liquid is well known. By contrast, in 2D systems melting is fundamentally different. This difference stems from the radical change of the intrinsic properties of matter in reduced dimensions. The long-range order which defines the periodic structure of a 3D crystal changes in 2D to only quasi-long-range translational (or positional) order [83,84].

According to the Kosterlitz–Thouless–Halperin–Nelson–Young (KTHNY) theory [85–88], a true 2D solid melts in two steps via two distinct successive phase transitions occurring at temperatures T_m and T_h, respectively. The intermediate hexatic phase is thereby characterized by the loss of translational order as for the liquid phase and by the subsistence of a certain degree of orientational order, in contrast to the liquid isotropic phase. For the melting of a 2D solid in the presence of a substrate potential, Nelson and Halperin predicted that the existence of the hexatic phase is hindered and melting directly occurs from the solid into the liquid phase [87].

Many experimental and numerical investigations have been devoted to study the melting transitions in 2D and to verify the KTHNY theory (for a review see [89]). The new class of 2D adatom superlattices, which are the subject of the present review, allows us to directly investigate the melting transition in two dimensions on the atomic scale.

We have seen that for Ce on Ag(1 1 1) the adatoms diffuse in the minimum of the superlattice potential already at 4.8 K (see Section 3.1). Therefore, for this kind of investigation the Ce/Ag(1 1 1) system is not a good choice because of the relatively large adatom–adatom distance and the relatively small interaction energy compared to the diffusion barrier which leads to a predicted melting temperature of only $T_m \lesssim 5$ K [67]. Thus, we have examined the temperature evolution of the superlattice of Ce adatoms on Cu(1 1 1) [67].

STM images obtained at a temperature of 8 K, 9 K and 14 K, respectively, are shown in Fig. 20a–c. At the elevated temperatures, the Ce adatoms become more mobile on the surface, inducing a modification of the apparent contrast between adatoms and aggregates. The gray-scale insets display the 2D Fourier transformation, corresponding to the structure factor of the positional data. Six sharp and distinct Bragg reflexes, signature of a 2D crystalline order, are observed at 8 K. At 9 K and 14 K the Bragg spots become more diffuse, and a ring appears, indicating melting of the 2D crystal. A weak hexagonal symmetry, however, is still visible in the Fourier transformation even at the elevated temperatures.

In a true 2D system the solid, hexatic, and liquid phases can be identified by a characteristic decay behavior of the pair correlation function $f(r)$, the density-density correlation function $g_r(r)$ and the bond-angular correlation function $g_6(r)$:

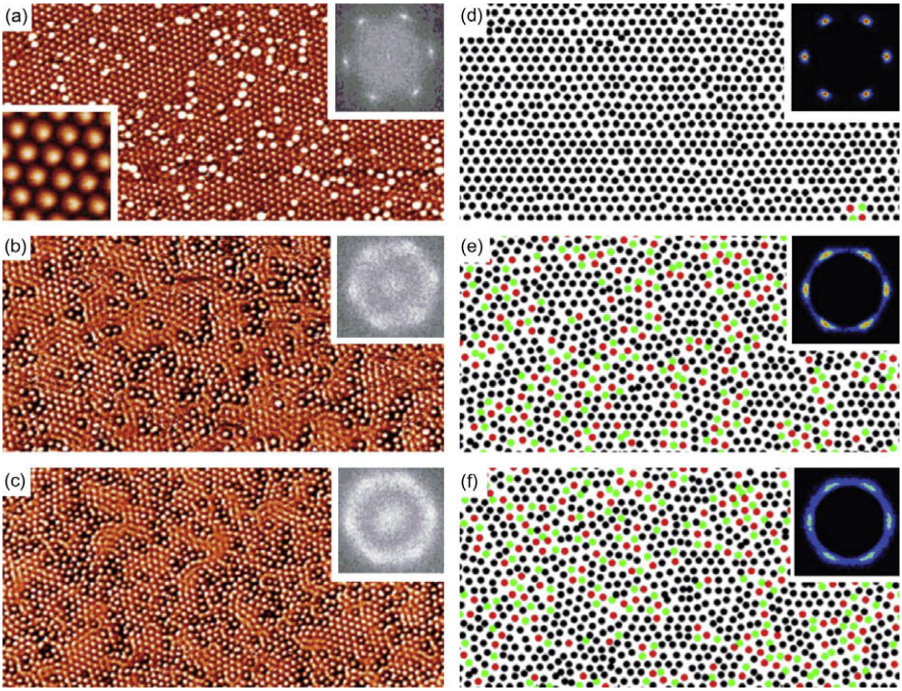

Fig. 20. (a-c) STM images (75×37 nm^2, $V = -20$ mV, $I = 20$ pA) acquired on Ce/Cu(1 1 1) for increasing temperatures T: (a) 8 K; (b) 9 K; (c) 14 K. About 0.04 ML of Ce adatoms form a macroscopic-ordered superlattice with an interatomic distance of 1.4 nm, as shown in the color inset to (a) (9.3×9.3 nm^2, $V = +1.8$ V, $I = 20$ pA). The grey-scale insets display the FT of each image. (d–f) Results of kMC simulations for about 0.04 ML Ce on Cu(1 1 1) at (a) 9 K; (b) 10 K; (c) 13 K. Black atoms are sixfold coordinated, red sevenfold, and green fivefold. The insets show the FT of each snapshot (adapted from [67]). (For interpretation of the references to colour in this figure legend, the reader is referred to the web version of this article.)

$$f(r) = \langle \sum_i \sum_{j\neq i} \delta(r - |\mathbf{r}_i - \mathbf{r}_j|)\rangle, \tag{14}$$

$$g_r(|\mathbf{r} - \mathbf{r}'|) =< \exp(i\mathbf{b}[\mathbf{u}(\mathbf{r}) - \mathbf{u}(\mathbf{r}')]) >, \tag{15}$$

$$g_6(|\mathbf{r} - \mathbf{r}'|) =< \exp(i6[\theta(\mathbf{r}) - \theta(\mathbf{r}')]) >, \tag{16}$$

where **b** denotes a reciprocal lattice vector of the superlattice, $\mathbf{u}(\mathbf{r})$ is the particle displacement field, $\theta(\mathbf{r})$ is the angle (with respect to a fix axis) of the bond centered at position **r**. The solid phase is characterized by a quasi-long range positional order and a long range orientational order, corresponding to an algebraic decay of $g_r(r)$ and to the absence of decay of $g_6(r)$ for $r \to \infty$. In the hexatic phase, the positional order is only short range, i.e. decays exponential, while the orientational order is quasi-long range (algebraic decay of $g_6(r)$). Finally, in the liquid phase both order parameters are short range, i.e. $g_r(r)$ and $g_6(r)$ decay exponentially.

The extraction of $g_r(r)$ from the experimental data is difficult because it would require a large number of STM images for each temperature. However, the pair correlation function was extracted from our data. For $T = 8$ K a power-law decay $f(r) \sim r^{-a}$ with $a \approx 0.9$ was found. For $T = 9$ and 14 K we observed an exponential decay, see Fig. 21a. This finding unambiguously shows that at 8 K the system is in the solid phase, while at $T \geqslant 9$ K the translational order is destroyed. The results for $g_6(r)$, deduced from the STM images of Fig. 20a–c and summarized in Fig. 21b, reveal that in the solid state at $T = 8$ K, $g_6(r)$ tends to a finite value in agreement with the prediction of the KTNHY theory. The behavior of $g_6(r)$ for 9 and 14 K, however, is not the one expected for a true 2D system: $g_6(r)$ approaches a constant value for large r, and does not decay to zero despite the fact that the translational order is destroyed.

An extensive theoretical investigation has been performed to clarify the 2D melting process for the Ce superlattice on Cu(1 1 1) [67]. The long-range interaction between two single Ce adatoms at different interatomic separations was deduced using *ab initio* density functional theory. This calculated long-range interaction potential was then used in a large-scale kinetic Monte-Carlo simulation [67] in which the surface was represented by a triangular lattice of equivalent fcc and hcp hollow sites.

The results obtained for different temperatures are presented in Fig. 20d–f. For $T = 8$ K a 2D ordered solid is formed by the Ce adatoms, as confirmed by the Fourier transformation in the inset. Almost all atoms are found to be sixfold coordinated (black color code). In the snapshots at elevated temperatures (Fig. 20e and f), the number of adatoms with six nearest neighbors decreases, while the amount of sevenfold (red) and fivefold (green) coordinated atoms increases. In the Fourier transformation of the images a ring appears, indicating that a melting transition has taken place. However, the hexagonal symmetry persists, with a striking resemblance to the experimental data of Fig. 20a–c.

Fig. 22a shows the density-density correlation function $g_r(r)$ obtained for the Ce/Cu(1 1 1) kinetic Monte-Carlo simulations at different temperatures. At temperatures $T \leqslant 9$ K, the system exhibits crystalline long-range order, as seen in the slow $r^{-\eta}$, $\eta < 0.1$ decay of $g_r(r)$. The melting of the 2D Ce lattice occurs between 9 and 10 K. Between these two temperatures the behavior of $g_r(r)$ changes dramatically – the correlation function decays exponentially above the melting temperature. In order to detect

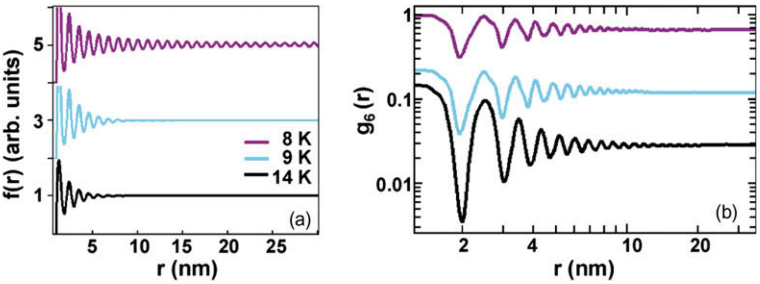

Fig. 21. (a) Pair correlation function $f(r)$ and (b) bond-angular correlation function $g_6(r)$ extracted from the experimental data shown in Fig. 20a–c (adapted from [67]).

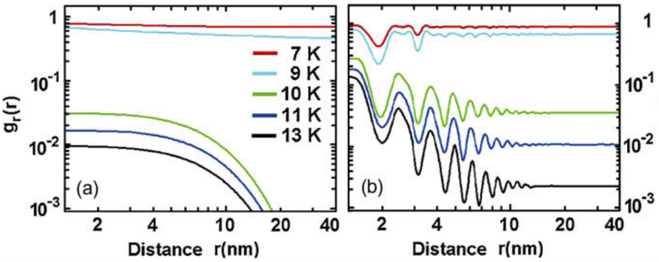

Fig. 22. (a) Density-density $g_r(r)$, (b) bond-angular $g_6(r)$ correlation functions calculated for about 0.04 ML of Ce on Cu(1 1 1) generated by kinetic Monte-Carlo simulations (adapted from [67]).

the hexatic phase, the analysis of the bond-angular correlation function $g_6(r)$ extracted for different temperatures and shown in Fig. 22b is required. In qualitative agreement with the results deduced from the experimental data, surprisingly $g_6(r)$ does not decay to zero at any temperature. In fact, these observations are in complete agreement with the predictions of Nelson and Halperin [87]: for the melting of a 2D crystal on a 'fine mesh' potential, (i) the existence of the hexatic phase is hindered and melting directly occurs from the solid into the liquid phase, (ii) in the liquid phase $g_6(r)$ tends to a finite value at large r and a substrate-induced hexagonal symmetry is present. According to the classification described by Nelson and Halperin [87], the superlattice of Ce/Cu(1 1 1) is (i) a commensurate solid at 7 K ($g_r(r) \sim r^{-\eta}, \eta = 0$), (ii) a floating solid at 9 K ($g_r(r) \sim r^{-\eta}, \eta = 0.09$), (iii) a fluid for $T \geqslant 10$ K.

For a Ce superlattice on Ag(1 1 1), a corresponding theoretical analysis has been performed in which the melting point T_m has been found to be between 4.5 K and 4.9 K [67]. The superlattice of Ce on Ag(1 1 1) constitutes a floating solid at 4.0 K ($\eta = 0.14$) and 4.5 K ($\eta = 0.18$), and becomes a fluid for $T \geqslant 4.9$ K. These findings demonstrate that the behavior of $g_6(r)$ is intrinsic to the Ce/Cu(1 1 1) and Ce/Ag(1 1 1) superlattices, i.e. the absence of hexatic phase is due to the substrate potential.

The critical parameters defining the surface potential are (i) the adatom diffusion barrier E_D and (ii) the periodicity, i.e. the separation between nearest adatoms in a superlattice d with respect to the mesh density r_0. For Ce on Cu(1 1 1) the ratio between $d = 1.3$ nm and $r_0 = 0.256$ nm sets the relative mesh density to ≈ 5. For Ce on Ag(1 1 1) the ratio is ≈ 11. In both cases, even in the liquid phase the Ce adatoms occupy discrete positions with respect to each other, and only a limited number of angles between two bonds are possible. Consequently, $g_6(r)$ does not decay to zero. In the limit of vanishing relative distance between neighboring adsorption sites (i.e. $d/r_0 \gg 1$), hexatic phase appears.

On the other hand, the diffusion barrier height E_D describes the 'flatness' of the surface. The comparison between E_D and the thermal energy of the adatom k_BT has to be considered. For $E_D < k_BT$, the adatom is not influenced by the substrate periodic potential, leading to diffusion on a flat surface: the adatom can be found at any point of the surface and not only in the hollow (adsorption) sites. Thus, at a typical temperature of $T = 10$ K, with $k_B = 0.086$ meV/K, the condition for the appearance of the hexatic phase corresponds to $E_D < 1$ meV.

However, as diffusion barriers $E_D < 1$ meV have not been observed, the considered class of atomic superlattices exemplarily demonstrates on the atomic scale the melting of a 2D solid in the presence of a weak substrate potential in which the hexatic phase does not exist and is thus confirming the predictions of the KTHNY theory.

4. Summary and outlook

The key parameters for successful self-assembly of adatom superlattices have been found to be the sample temperature, a relatively low adatom diffusion barrier and the adatom concentration. A subtle balance of these parameters is decisive for the formation of a superlattice. The adatoms need sufficient thermal energy to overcome the outer repulsive potential barriers and they have to be present in sufficient concentration to form the necessary potential well depth to lock in the first minimum at nearest neighbor distance in their search for the deepest minimum in the long-range attractive potential well.

The structural long-range order of the adatom superlattice is found to depend on the number of adatom dimers on the surface, which is related to the natural superlattice parameters. Stepanyuk et al. found a quantitative expression for this behavior. For example, the difference between the self-organization of Co adatoms on Cu(1 1 1) and Ce adatoms on Ag(1 1 1) is determined by the formation of dimers during or after deposition. The concentration of dimers at the optimal coverage depends on the relative position of the first maximum a and the first minimum b in the long-range interaction potential $\Gamma = a/b$ [75]. A smaller value of Γ corresponds to a smaller concentration of dimers. For Co atoms on Cu(1 1 1) a value of $\Gamma = 0.45$ is found. As a consequence a significant number of immobile dimers prevents the efficient self-assembly of the randomly distributed adatoms towards a superlattice. For Ce on Ag(1 1 1) a value of $\Gamma = 0.16$ is obtained. This relatively small value corresponds to a significantly lower ad-dimer concentration on the surface which permits the formation of a well-ordered Ce-adatom superlattice. A general rule of thumb resulting from this discussion would read as follows. The larger the superlattice adatom–adatom distance, the lesser dimers will form and the better the adatom superlattice order will be.

There are different routes for tuning the superlattice constant. (i) On a given substrate supporting a surface state, the adatom–adatom distance within the superlattice can be changed by varying the adatom concentration. For Ce on Ag(1 1 1) this recipe led to Ce–Ce distances between $d = 2.3$—3.5 nm [80]. (ii) By changing the single crystal substrate, i.e., in going from Ag(1 1 1) to Cu(1 1 1) owing to the difference in Fermi wave vector of the surface state electrons, the superlattice constant changes from 3.2 nm to 1.4 nm [45,67]. (iii) On epitaxial ultrathin films, the development of a thickness-dependent surface state has been reported, for example for Ag layers grown on Cu(1 1 1) [90]. (iv) An interesting possible future research direction would be the study of superlattice formation on metal alloys and on semiconductor surfaces supporting a surface state. For example, in CuAl alloys with well defined single crystal lattice faces, the Fermi wavelength λ of the Cu surface state electrons changes with the Cu concentration from the Cu(1 1 1) surface with $\lambda = 2.8$ nm to $\lambda = 2.2$ nm on (1×1)-CuAl and to $\lambda = 1.8$ nm on $(\sqrt{3} \times \sqrt{3})$-CuAl [91].

Owing to the surface-state-mediated interactions between the Ce adatoms, a relatively wide 2D superlattice is created, providing us with the exciting opportunity to measure the distribution of electronic states directly inside the lattice. We have seen that the density of states varies depending on the site in the superlattice. At the Fermi energy E_F the LDOS vanishes leading to a gap opening which is essential for the superlattice stability. These results are surprising in the light of the discussion of the scattering model (Section 3.1) which assumes that electrons at the Fermi edge are an important ingredient for the realization of the long-range adatom interaction. However, when the superlattice is completed, there are no surface-state electrons at the Fermi energy that could perform this interaction.

The magnetic moment of the 3d and 4f-electrons leads to an additional degree of freedom which is expected to cause adatom–adatom interactions between the magnetic moments, the so called Ruderman–Kittel–Kasuya–Yosida (RKKY) exchange interaction [92–94], which has in 2D a periodicity of $\lambda_F/2$ [95–97] and a $1/r^2$ behavior, similar to the discussed adatom–adatom interaction induced by electron scattering. Therefore spin-resolved STS measurements could reveal the magnetic order in such superlattices, in a similar fashion as has been demonstrated convincingly for Co adatoms on Pt(1 1 1) [98]. Other systems, for example Fe/Cu(1 1 1) [65,72] or Mn/Cu(1 1 1) [99] may be good candidates for the detection of spin-polarized surface-state-mediated interactions between the magnetic moments of the adatoms.

The peculiar electronic structure of cerium, where the hybridization of the highly localized 4f-state of Ce [100] with bulk and surface state electrons is at the heart of Kondo physics [101] was not taken into account in this review. As the Kondo effect leads to characteristic signatures in the tunneling spectra [102–104], ordered 2D superlattices with partially screened and/or partially interacting magnetic moments are a promising research field for low-temperatures STS. As this kind of superlattices may represent a 2D Kondo lattice [105] or may display antiferromagnetic order and superconductivity [106], spectroscopic investigations on a local scale within these superlattices would give new insights in such collective phenomena.

On the other hand, depending on the magnetocrystalline anisotropy, the adatoms in the superlattice may leave the Kondo regime and develop stable, yet switchable magnetic moments, a property of high interest for electron-spin based quantum computing.

To summarize, the ability to control the long-range order of magnetic adatoms opens new possibilities and presents new challenges for the investigation of two-dimensional magnetism and for the development of novel atomic-scale magnetic devices.

Acknowledgements

The authors would like to thank J.P. Pelz, F. Silly, F. Mila, C. Weber, T. Giamarchi, N.N. Negulyaev, V.S. Stepanyuk, L. Niebergall, and P. Bruno for stimulating discussions and for a very fruitful collaboration. We acknowledge the financial support by the Swiss National Science Foundation. WDS would like to acknowledge the outstanding hospitality of the Stiftung Dr. Robert und Lina Thyll-Dürr, where part of this manuscript has been written: 2008-Arbeitsaufenthalt in der Casa Zia Lina, Elba, als Gast der Stiftung Dr. Robert und Lina Thyll-Dürr (Schweiz).

References

[1] N.P. Mahalik (Ed.), Micromanufacturing and Nanotechnology, Springer, Berlin, 2006.
[2] D.M. Eigler, E.K. Schweizer, Positioning single atoms with a scanning tunnelling microscope, Nature 344 (1990) 524.
[3] H.C. Manoharan, C.P. Lutz, D.M. Eigler, Quantum mirages formed by coherent projection of electronic structure, Nature 403 (2000) 512.
[4] A.J. Heinrich, C.P. Lutz, J.A. Gupta, D.M. Eigler, Molecule cascades, Science 298 (2002) 1381.
[5] N. Nilius, T.M. Wallis, W. Ho, Development of one-dimensional band structure in artificial gold chains, Science 297 (2002) 1853.
[6] N. Oyabu, Y. Sugimoto, M. Abe, O. Custance, S. Morita, Lateral manipulation of single atoms at semiconductor surfaces using atomic force microscopy, Nanotechnology 16 (2005) S112.
[7] M. Ternes, C.P. Lutz, C.F. Hirjibehedin, F.J. Giessibl, A.J. Heinrich, The force needed to move an atom on a surface, Science 319 (2008) 1066.
[8] G.M. Whitesides, B. Grzybowski, Self-assembly at all scales, Science 295 (2002) 2418.
[9] H. Zeng, J. Li, J.P. Liu, Z.L. Wang, S. Sun, Exchange-coupled nanocomposite magnets by nanoparticle self-assembly, Nature 420 (2002) 395.
[10] C.T. Black, C.B. Murray, R.L. Sandstrom, S. Sun, Spin-dependent tunneling in self-assembled cobalt-nanocrystal superlattices, Science 290 (2000) 5494.
[11] H. Brune, Superlattices of atoms, molecules and islands, in: Single Molecules at Surfaces, Springer, New York, 2006, pp. 247–267.
[12] M. Becker, K. Wandelt, Surfaces: Two-Dimensional Templates, Springer, Berlin, Heidelberg, 2008.
[13] T.L. Einstein, J.R. Schrieffer, Indirect interaction between adatoms on a tight-binding solid, Phys. Rev. B 7 (1973) 3629.
[14] K.H. Lau, W. Kohn, Elastic interaction of two atoms adsorbed on a solid surface, Surf. Sci. 65 (1977) 607.
[15] O.M. Braun, V.K. Medvedev, Interaction between particles adsorbed on metal surfaces, Sov. Phys. Usp. 32 (1989) 328.
[16] K.A. Fichthorn, M. Scheffler, Island nucleation in thin-film epitaxy: a first-principles investigation, Phys. Rev. Lett. 84 (2000) 5371.
[17] A. Bogicevic, S. Ovesson, P. Hyldgaard, B.I. Lundqvist, H. Brune, D.R. Jennison, Nature, strength, and consequences of indirect adsorbate interactions on metals, Phys. Rev. Lett. 85 (2000) 1910.
[18] K.A. Fichthorn, M.L. Merrick, M. Scheffler, Nanostructures at surfaces from substrate–mediated interactions, Phys. Rev. B 68 (2003) 041404.
[19] M.L. Merrick, W. Luo, K.A. Fichthorn, Substrate–mediated interactions on solid surfaces: theory, experiment, and consequences for thin-film morphology, Prog. Surf. Sci. 72 (2003) 117.
[20] W. Kohn, K.H. Lau, Adatom dipole moments on metals and their interactions, Solid State Commun. 18 (1976) 553.
[21] K.H. Lau, W. Kohn, Indirect long-range oscillatory interaction between adsorbed atoms, Surf. Sci. 75 (1978) 69.
[22] J. Koutecký, A contribution to the molecular-orbital theory of chemisorption, Trans. Faraday Soc. 54 (1958) 1038.
[23] J. Friedel, Metallic alloys, Nuovo Cim. Suppl. 7 (1958) 287.
[24] T.B. Grimley, The indirect interaction between atoms or molecules adsorbed on metals, Proc. Phys. Soc. 90 (1967) 751.
[25] T.B. Grimley, The electron density in a metal near a chemisorbed atom or molecule, Proc. Phys. Soc. 92 (1967) 776.
[26] T.L. Einstein, Comment on 'oscillatory indirect interaction between adsorbed atoms – non-asymptotic behavior in tight-binding models at realistic parameters', in: K.H. Lau, W. Kohn (Eds.), Surf. Sci. 75 (1978) 161.
[27] T.T. Tsong, Field-ion microscope observations of indirect interaction between adatoms on metal surfaces, Phys. Rev. Lett. 31 (1973) 1207.
[28] W.C. Fan, A. Ignatiev, Ordered phases and phase transitions of cesium on the Cu(111) surface, J. Vac. Sci. Technol. A 6 (1988) 735.
[29] G. Alexandrowicz, A.P. Jardine, H. Hedgeland, W. Allison, J. Ellis, Onset of 3d collective surface diffusion in the presence of lateral interactions: Na/Cu(001), Phys. Rev. Lett. 97 (2006) 156103.
[30] W. Shockley, On the surface states associated with a periodic potential, Phys. Rev. 56 (1939) 317.
[31] A. Zangwill, Physics at Surfaces, Cambridge University Press, Cambridge, 1988.

[32] J.T. Li, W.D. Schneider, R. Berndt, Local density of states from spectroscopic scanning–tunneling-microscope images: Ag(1 1 1), Phys. Rev. B 56 (1997) 7656.
[33] J.T. Li, W.D. Schneider, R. Berndt, O.R. Bryant, S. Crampin, Surface-state lifetime measured by scanning tunneling spectroscopy, Phys. Rev. Lett. 81 (1998) 4464.
[34] J. Kliewer, R. Berndt, E.V. Chulkov, V.M. Silkin, P.M. Echenique, S. Crampin, Dimensionality effects in the lifetime of surface states, Science 288 (2000) 1399.
[35] M. Pivetta, F. Silly, F. Patthey, J.P. Pelz, W.D. Schneider, Reading the ripples of confined surface-state electrons: profiles of constant integrated local density of states, Phys. Rev. B 67 (2003) 193402.
[36] P.M. Echenique, R. Berndt, E.V. Chulkov, Th. Fauster, A. Goldmann, U. Hofer, Decay of electronic excitations at metal surfaces, Surf. Sci. Rep. 52 (2004) 219.
[37] J. Tersoff, D.R. Hamann, Theory of the scanning tunneling microscope, Phys. Rev. B 31 (1985) 805.
[38] N.D. Lang, Spectroscopy of single atoms in the scanning tunneling microscope, Phys. Rev. B 34 (1986) 5947.
[39] L. Bürgi, O. Jeandupeux, H. Brune, K. Kern, Probing hot-electron dynamics at surfaces with a cold scanning tunneling microscope, Phys. Rev. Lett. 82 (1999) 4516.
[40] L.C. Davis, M.P. Everson, R.C. Jaklevic, Theory of the local density of surface states on a metal: comparison with scanning tunneling spectroscopy of a Au(1 1 1) surface, Phys. Rev. B 43 (1991) 3821.
[41] M.F. Crommie, C.P. Lutz, D.M. Eigler, Imaging standing waves in a 2-dimensional electron gas, Nature 363 (1993) 524.
[42] P. Avouris, I.W. Lyo, Observation of quantum-size effects at room temperature on metal surfaces with STM, Science 264 (1994) 942.
[43] Y. Hasegawa, Ph. Avouris, Direct observation of standing wave formation at surface steps using scanning tunneling spectroscopy, Phys. Rev. Lett. 71 (1993) 1071.
[44] N.W. Ashcroft, N.D. Mermin, Solid State Physics, HRW, Philadephia, 1976.
[45] F. Silly, M. Pivetta, M. Ternes, F. Patthey, J.P. Pelz, W.D. Schneider, Creation of an atomic superlattice by immersing metallic adatoms in a two-dimensional electron sea, Phys. Rev. Lett. 92 (1) (2004) 016101.
[46] P. Hyldgaard, M. Persson, Long-ranged adsorbate–adsorbate interactions mediated by a surface-state band, J. Phys.: Condens. Matter 12 (2000) L13.
[47] E. Wahlstrom, I. Ekvall, H. Olin, L. Wallden, Long-range interaction between adatoms at the Cu(1 1 1) surface imaged by scanning tunnelling microscopy, Appl. Phys. A 66 (1998) S1107.
[48] J. Repp, F. Moresco, G. Meyer, K.H. Rieder, P. Hyldgaard, M. Persson, Substrate mediated long-range oscillatory interaction between adatoms: Cu/Cu(1 1 1), Phys. Rev. Lett. 85 (2000) 2981.
[49] N. Knorr, H. Brune, M. Epple, A. Hirstein, M.A. Schneider, K. Kern, Long-range adsorbate interactions mediated by a two-dimensional electron gas, Phys. Rev. B 65 (2002) 115420.
[50] F. Silly, M. Pivetta, M. Ternes, F. Patthey, J.P. Pelz, W.D. Schneider, Coverage-dependent self-organization: from individual adatoms to adatom superlattices, New J. Phys. 6 (2004) 16.
[51] J. Harris, Simplified method for calculating the energy of weakly interacting fragments, Phys. Rev. B 31 (1985) 1770.
[53] L.D. Schmidt, R. Gomer, Adsorption of potassium on tungsten: measurements on single-crystal planes, J. Chem. Phys. 45 (1966) 1605.
[54] M. Ziegler, J. Kröger, R. Berndt, A. Filinov, M. Bonitz, Scanning tunneling microscopy and kinetic Monte Carlo investigation of cesium superlattices on Ag(1 1 1), Phys. Rev. B 78 (2008) 245427.
[55] J. Zhao, M. Pontius, A. Winkelmann, V. Sametoglu, A. Kubo, A.G. Borisov, D. Sánchez-Portal, V.M. Silkin, E.V. Chulkov, P.M. Echenique, H. Petek, Electronic potential of a chemisorption interface, Phys. Rev. B 78 (2008) 085419.
[56] P. Hyldgaard, T.L. Einstein, Surface-state-mediated three-adsorbate interaction, Europhys. Lett. 59 (2002) 265.
[57] V.S. Stepanyuk, A.N. Baranov, D.V. Tsivlin, W. Hergert, P. Bruno, N. Knorr, M.A. Schneider, K. Kern, Quantum interference and long-range adsorbate–adsorbate interactions, Phys. Rev. B 68 (2003) 205410.
[58] N.N. Negulyaev, V.S. Stepanyuk, W. Hergert, H. Fangohr, P. Bruno, Effect of the long-range adsorbate interactions on the atomic self-assembly on metal surfaces, Surf. Sci. 600 (2006) L58.
[59] J.M. Rogowska, M. Maciejewski, Dilute Cu nanostructure stabilized by substrate–mediated interactions on Cu(1 1 1): kinetic Monte Carlo simulations, Phys. Rev. B 74 (2006) 235402.
[60] J. Hu, B. Teng, F. Wu, Y. Fang, Fe nanostructures stabilized by long-range interactions on Cu(1 1 1): kinetic Monte Carlo simulations, New J. Phys. 10 (2008) 023033.
[61] M. Kulawik, H.P. Rust, M. Heyde, N. Nilius, B.A. Mantooth, P.S. Weiss, H.J. Freund, Interaction of CO molecules with surface state electrons on Ag(1 1 1), Surf. Sci. 590 (2005) L253.
[62] S.U. Nanayakkara, E.C.H. Sykes, M.M. Blake, L.C. Fernandez-Torres, P.S. Weiss, Long-range electronic interactions at a high temperature: bromine adatom islands on Cu(1 1 1), Phys. Rev. Lett. 98 (2007) 206108.
[63] G. Manai, K. Radican, F. Delogu, I.V. Shvets, Room-temperature self-assembly of equilateral triangular clusters via Friedel oscillations, Phys. Rev. Lett. 101 (2008) 165701.
[64] N.N. Negulyaev, V.S. Stepanyuk, L. Niebergall, W. Hergert, H. Fangohr, P. Bruno, Self-organization of Ce adatoms on Ag(1 1 1): a kinetic Monte Carlo study, Phys. Rev. B 74 (2006) 035421.
[65] V.S. Stepanyuk, L. Niebergall, R.C. Longo, W. Hergert, P. Bruno, Magnetic nanostructures stabilized by surface-state electrons, Phys. Rev. B 70 (2004) 075414.
[66] M. Ternes. Scanning Tunneling Spectroscopy at the Single Atom Scale. PhD thesis, École Polytechnique Fédérale de Lausanne, 2006. <http://library.epfl.ch/en/theses/?nr=3465>.
[67] N.N. Negulyaev, V.S. Stepanyuk, L. Niebergall, P. Bruno, M. Pivetta, M. Ternes, F. Patthey, W.D. Schneider, Melting of two-dimensional adatom superlattices stabilized by long-range electronic interactions, Phys. Rev. Lett. 102 (2009) 246102.
[68] Th. von Hofe, J. Kroger, R. Berndt, Adsorption geometry of Cu(1 1 1)-Cs studied by scanning tunneling microscopy, Phys. Rev. B 73 (2006) 245434.
[69] M. Ziegler, J. Kröger, R. Berndt, A.G. Borisov, J.P. Gauyacq, Linewidth of a cesium adatom resonance on Ag(1 1 1), Phys. Rev. B 79 (2009) 075401.
[70] T. Yokoyama, T. Takahashi, K. Shinozaki, Quantitative analysis of long-range interactions between adsorbed dipolar molecules on Cu(1 1 1), Phys. Rev. Lett. 98 (2007) 206102.

[71] I. Fernandez-Torrente, S. Monturet, K.J. Franke, J. Fraxedas, N. Lorente, J.I. Pascual, Long-range repulsive interaction between molecules on a metal surface induced by charge transfer, Phys. Rev. Lett. 99 (2007) 176103.
[72] N.N. Negulyaev, V.S. Stepanyuk, L. Niebergall, P. Bruno, W. Auwärter, Y. Pennec, G. Jahnz, J.V. Barth, Effect of strain relaxations on heteroepitaxial metal-on-metal island nucleation and superlattice formation: Fe on Cu(1 1 1), Phys. Rev. B 79 (2009) 195411.
[73] S. Pick, V.S. Stepanyuk, A.L. Klavsyuk, L. Niebergall, W. Hergert, J. Kirschner, P. Bruno, Magnetism and structure on the atomic scale: small cobalt clusters in Cu(0 0 1), Phys. Rev. B 70 (2005) 224419.
[74] V.S. Stepanyuk, A.N. Baranov, W. Hergert, P. Bruno, Ab initio study of interaction between magnetic adatoms on metal surfaces, Phys. Rev. B 68 (2003) 205422.
[75] V.S. Stepanyuk, N.N. Negulyaev, L. Niebergall, P. Bruno, Effect of quantum confinement of surface electrons on adatom–adatom interactions, New J. Phys. 9 (2007) 388.
[76] M.F. Crommie, C.P. Lutz, D.M. Eigler, Confinement of electrons to quantum corrals on a metal surface, Science 262 (1993) 218.
[77] V.S. Stepanyuk, N.N. Negulyaev, L. Niebergall, R.C. Longo, P. Bruno, Adatom self-organization induced by quantum confinement of surface electrons, Phys. Rev. Lett. 97 (2006) 186403.
[78] A. Schiffrin, J. Reichert, W. Auwärter, G. Jahnz, Y. Pennec, A. Weber-Bargioni, V.S. Stepanyuk, L. Niebergall, P. Bruno, J.V. Barth, Self-aligning atomic strings in surface-supported biomolecular gratings, Phys. Rev. B 78 (2008) 035424.
[79] C. Liu, T. Uchihashi, T. Nakayama, Self-alignment of Co adatoms on in atomic wires by quasi-one-dimensional electron–gas-meditated interactions, Phys. Rev. Lett. 101 (2008) 146104.
[80] M. Ternes, C. Weber, M. Pivetta, F. Patthey, J.P. Pelz, T. Giamarchi, F. Mila, W.D. Schneider, Scanning-tunneling spectroscopy of surface-state electrons scattered by a slightly disordered two-dimensional dilute solid: Ce on Ag(1 1 1), Phys. Rev. Lett. 93 (2004) 146805.
[81] J.T. Li, W.D. Schneider, R. Berndt, O.R. Bryant, S. Crampin, Electron confinement to nanoscale Ag islands on Ag(1 1 1): a quantitative study, Phys. Rev. Lett. 80 (1998) 3332.
[82] L.R. Gor'kov, G. Grüner (Eds.), Charge Density Waves in Solids, Elsevier, Amsterdam, 1989.
[83] N.D. Mermin, H. Wagner, Absence of ferromagnetism or antiferromagnetism in one- or two-dimensional isotropic Heisenberg models, Phys. Rev. Lett. 17 (1966) 1133.
[84] N.D. Mermin, Crystalline order in two dimensions, Phys. Rev. 176 (1968) 250.
[85] J.M. Kosterlitz, N.J. Thouless, Ordering, metastability and phase transitions in two-dimensional systems, J. Phys. C 6 (1973) 1181.
[86] B.I. Halperin, D.R. Nelson, Theory of two-dimensional melting, Phys. Rev. Lett. 41 (1978) 121.
[87] D.R. Nelson, B.I. Halperin, Dislocation-mediated melting in two dimensions, Phys. Rev. B 19 (1979) 2484.
[88] A.P. Young, Melting and the vector Coulomb gas in two dimensions, Phys. Rev. B 19 (1979) 1855.
[89] K.J. Strandburg, Two-dimensional melting, Rev. Mod. Phys. 60 (1988) 161.
[90] A. Bendounan, H. Cercellier, Y. Fagot-Revurat, B. Kierren, V. Yurov, D. Malterre, Modification of Shockley states induced by surface reconstruction in epitaxial Ag films on Cu(1 1 1), Phys. Rev. B 67 (2003) 165412.
[91] H. Asonen, M. Lindroos, M. Pessa, R. Prasad, R.S. Rao, A. Bansil, Angle-resolved photoemission study of (1 0 0), (1 1 0), and (1 1 1) surfaces of $Cu_{0.9}Al_{0.1}$: bulk and surface electronic structure of the alloy, Phys. Rev. B 25 (1982) 7075.
[92] M.A. Ruderman, C. Kittel, Indirect exchange coupling of nuclear magnetic moments by conduction electrons, Phys. Rev. 96 (1954) 99.
[93] T. Kasuya, A theory of metallic ferro- and antiferromagnetism on Zener's model, Prog. Theor. Phys. 16 (1956) 45.
[94] K. Yosida, Magnetic properties of Cu–Mn alloys, Phys. Rev. 106 (1957) 893.
[95] B. Fischer, M.W. Klein, Magnetic and nonmagnetic impurities in two-dimensional metals, Phys. Rev. B 11 (1975) 2025.
[96] M.T. Beal-Monod, Ruderman–Kittel–Kasuya–Yosida indirect interaction in two dimensions, Phys. Rev. B 36 (1987) 8835.
[97] V.I. Litvinov, V.K. Dugaev, RKKY interaction in one- and two-dimensional electron gases, Phys. Rev. B 58 (1998) 3584.
[98] F. Meier, L. Zhou, J. Wiebe, R. Wiesendanger, Revealing magnetic interactions from single-atom magnetization curves, Science 320 (2008) 82.
[99] C.F. Hirjibehedin, C.P. Lutz, Private communication.
[100] B.N. Harmon, A.J. Freeman, Spin-polarized energy-band structure, conduction–electron polarization, spin densities, and the neutron magnetic form factor of ferromagnetic gadolinium, Phys. Rev. B 10 (1974) 1979.
[101] J. Kondo, Resistance minimum in dilute magnetic alloys, Prog. Theor. Phys. 32 (1964) 37.
[102] J.T. Li, W.D. Schneider, R. Berndt, B. Delley, Kondo scattering observed at a single magnetic impurity, Phys. Rev. Lett. 80 (1998) 2893.
[103] V. Madhavan, W. Chen, T. Jamneala, M.F. Crommie, N.S. Wingreen, Tunneling into a single magnetic atom: spectroscopic evidence of the Kondo resonance, Science 280 (1998) 567.
[104] M. Ternes, A.J. Heinrich, W.D. Schneider, Spectroscopic manifestations of the Kondo effect on single adatoms, J. Phys.: Condens. Matter 21 (2009) 053001.
[105] H. Tsunetsugu, M. Sigrist, K. Ueda, The ground-state phase diagram of the one-dimensional Kondo lattice model, Rev. Mod. Phys. 69 (1997) 809.
[106] C. Weber, A. Laeuchli, F. Mila, T. Giamarchi, Magnetism and superconductivity of strongly correlated electrons on the triangular lattice, Phys. Rev. B 73 (2006) 014519.